An *hp*-adaptive discontinuous Galerkin method for phase field fracture

Robert E. Bird[a],[*], Charles E. Augarde[a], William M. Coombs[a], Ravindra Duddu[c],
Stefano Giani[a], Phuc T. Huynh[b], Bradley Sims[a]

[a] *Department of Engineering, Durham University, UK*
[b] *CIRTECH Institute, Ho Chi Minh City University of Technology (HUTECH), Ho Chi Minh City, Viet Nam*
[c] *Department of Civil and Environmental Engineering, Vanderbilt University, USA*

Abstract

The phase field method is becoming the *de facto* choice for the numerical analysis of complex problems that involve multiple initiating, propagating, interacting, branching and merging fractures. However, within the context of finite element modelling, the method requires a fine mesh in regions where fractures will propagate, in order to capture sharp variations in the phase field representing the fractured/damaged regions. This means that the method can become computationally expensive when the fracture propagation paths are not known *a priori*. This paper presents a 2D *hp*-adaptive discontinuous Galerkin finite element method for phase field fracture that includes *a posteriori* error estimators for both the elasticity and phase field equations, which drive mesh adaptivity for static and propagating fractures. This combination means that it is possible to be reliably and efficiently solve phase field fracture problems with arbitrary initial meshes, irrespective of the initial geometry or loading conditions. This ability is demonstrated on several example problems, which are solved using a light-BFGS (Broyden–Fletcher–Goldfarb–Shanno) quasi-Newton algorithm. The examples highlight the importance of driving mesh adaptivity using both the elasticity and phase field errors for physically meaningful, yet computationally tractable, results. They also reveal the importance of including *p*-refinement, which is typically not included in existing phase field literature. The above features provide a powerful and general tool for modelling fracture propagation with controlled errors and degree-of-freedom optimised meshes.

1. Introduction

The phase field model for brittle fracture originally proposed by [1,2] describes crack propagation based on Griffith's theory. Unlike linear elastic fracture mechanics, the phase field model for fracture is a type of non-local continuum damage model, where the crack is defined by a diffused damage zone rather than a sharp (zero-thickness)

* Corresponding author.
  E-mail address: robert.e.bird@durham.ac.uk (R.E. Bird).

discontinuity. Material failure is characterised by a constitutive damage relation arising from variational [2] or thermodynamic arguments [3]. Since the primary phase field equation approximates the fracture topology as a field, cracks naturally initiate, branch and merge. This is a notable advantage over discrete fracture mechanics, where the fractures are modelled through boundary topology, and does not naturally incorporate these features in the continuum framework. The algorithmic implementation, especially in 3D, of discrete crack topology changes, such as branching and merging, is challenging but remeshing is an option in order to capture the evolution of the crack topology [4]. Additionally determining when, and then how, cracks split and initiate is not implicit to the fundamental principle of discrete crack propagation. Thermodynamic frameworks for discrete fracture propagation are often cast as a single crack tip, or front, [5]. Alternatively, the phase field model is both difficult to solve, requiring many iterations per load step, and are significant refinement along the entire damaged region, representing the crack, [6], unlike discrete methods where only tip refinement is required [e.g.,7]. It therefore can be prohibitively expensive for large 3D simulations. For example, simulating fracture propagation using the phase field model in glaciers and ice shelves [8,9] that are several hundred kilometres long requires metre-scale resolution within damage zones. Therefore, in order to model phase field fracture, significant manual intervention is required to refine the domain based on the anticipated crack path, which can be computationally inefficient, or worse could miss fractures that are not expected *a priori*.

Mesh adaptivity has the capability to create efficient solution dependent meshes and automatically detect regions of crack initiation. Since the most difficult regions of the field to model are likely associated with phase field values representing the crack, the field values are often used as a primary driver, or error indicator, in mesh adaptivity [10,11]. For example, a commonly adopted scheme, [12–16] amongst others, is the predictor–corrector method, [17,18], where a region around the damaged material is used to identify elements to refine. A similar but alternative method is to use threshold values for the positive strain energy as markers [19–21], or through a physical stability measure to refine elements which are at the onset of fracture [22]. The advantage of these methods is that they have the potential to refine elements before they fracture, thus minimising rerunning load steps. In addition to mesh adaptivity are schemes which aim to reduce the computational cost, for example global-local formulations exist where the phase field solution is resolved locally to the crack path, [15]. A similar approach is presented by Muixí et al. [23], where in regions of the crack path away from developing regions of the phase field an XFEM enrichment is introduced to remove the requirement for high levels of refinement along the complete crack path.

A posteriori error estimators have been used for a range of problems, from discrete fracture [24], reaction–diffusion equations [25] and phase-field fracture. There are several types of error estimators available which have been applied to phase-field fracture propagation. The works of [26–28] use a recovery type error estimator [29], where a refined, or higher order, mesh is used to estimate the error. Alternatively there are goal-orientated error estimators in which the error is estimated for a quantity of interest using an adjoint solution on a higher order mesh. This has been applied to phase field fracture in [30,31] where errors for the elastic phase field solutions, and those associated with the time step size, have been estimated. The error that is used here is a residual type which has the advantage that the error measure is a function of only the primal solution on the mesh it is solved on, therefore no further solutions are required to determine the error. This type of estimator was applied approximately by Mang et al. [32] to errors in the phase field problem, and robustly by Burke et al. [33,34] and Micheletti et al. [35] to the Ambrosio–Tortorelli formulation with h-adaptivity. Here a robust residual *a posteriori* hp-error estimator is applied to phase-field fracture. For an estimator to be defined as robust it must bound from above (reliable) and below (efficient) the true error in the problem's energy norm, up to some constants independent of element size and polynomial order. This means the estimate is never too far away from the true error and is therefore a good measure of the error distribution through the computational mesh [36]. It also means the convergence rate of the estimate is approximately the same as the true error. This definition of robust is used throughout the paper. The hp-error estimator proposed in this paper is applicable to meshes which contain elements of arbitrary size and polynomial order. Since the error estimate bounds the error in the hp-discontinuous Galerkin (DG) energy norm and the solutions space for continuous Galerkin (CG) is a subspace of the DG solution space, the error estimator is also directly applicable to hp-CG formulations. The error estimator methods discussed in this section and presented in later sections, can be wrapped around existing numerical frameworks. However, some methods such as the discontinuous Petrov–Galerkin (PDG) method have *"a built-in error evaluator"* [37,38] used as an error estimator to guide refinement.

An additional difficultly is that the coupled phase field fracture problem is non-convex with respect to the primary displacement and phase field variables [39,40]. However, it was recognised by [2], that the problem is convex

when taking variations of the energy functional with respect to only one of the primary variables, leading to the development of the robust Alternate Minimisation (AM) scheme [2] and later the staggered scheme [41]. Although both are robust, the staggered scheme is highly dependent on the load step size and the AM scheme is slow to converge [42]. This has lead to the adaptation of a series of non-linear solvers to the phase field fracture framework: such as the Gauss–Seidel method which is an accelerated approach to the AM approach [42]; traditional Newton solvers with robust line searches, positive and negative search directions [40]; quasi-Newton methods which avoid computations of the secant matrix each step and reduce the number of iterations compared to AM [39,43]; an under-relaxation arc-length method which enables larger displacement steps whilst accurately capturing the instantaneous crack growth [44]; and the implicit–explicit method [45] which uses an implicit method before damage localisation and an explicit dynamics solver is used during fracture. Lastly, multigrid preconditioner methods [46], and domain decomposition preconditioners [47] for dynamic problems solved in parallel, have been used to reduce memory load and overall computational time.

Many of the above approaches use a CG framework, although finite difference [48] and Fast Fourier Transform [49] implementations exist. However as an alternative there are authors who use either DG or hybridised DG frameworks [11,50–52]. The DG solution space is a broken Sobolev space, the primary variables are discontinuous between adjacent elements but continuous within elements. Degrees of freedom (DOF) are therefore not shared between adjacent elements and communication between elements is through face integrals. Here hp-adaptivity is used to efficiently obtain accurate solutions of the phase-field method. The DG method is used since any jumps in element size (with hanging nodes) and polynomial order are naturally incorporated in face integrals between elements. In the authors' opinion this is considered algorithmically simpler than hp-CG methods. Compared to hp-DG methods, the hp-CG trades the computational effort of DG face integrals with the additional treatment to ensure conforming polynomial orders on the edges shared between elements in conforming meshes. However, some authors do consider it is algorithmically simpler to ensure that the mesh conforms [53,54], with the additional benefit that for the same mesh, CG requires fewer degrees of freedom. For a detailed explanation of the theoretical and algorithmic aspects for arbitrary elements in hp-CG see Solin [55]. For Cartesian meshes, see [56] for Isogeometric Analysis hp-FEM and [57] for methods considering hanging nodes. Nevertheless computational cost is not purely measured on the number of DOF and the methods do have different solution spaces. This means for a problem one method might outperform the other for a similar cost.

An aspect of the phase field fracture method which is often overlooked is the smoothness of the phase field solution and the possibility of p-adaptivity being used to resolve smooth regions, [58]. In comparison to h-adaptivity relatively few authors consider hp-adaptivity, for instance, Muixi et al. [50] uses a uniform hp-refined patch. This is based on a phase field marking criteria, and [53,54] use a error indicator to identify which regions of the mesh to perform hp-adaptivity, in both 2D and 3D. However, an error driven hp-adaptivity method has not been presented in the literature, to the best of the authors' knowledge.

This paper provides a hp-adaptive DG modelling framework based on a robust hp-residual *a posteriori* based error estimator for the phase field solution and uses the hp-residual *a posteriori* error estimator for elasticity from [36]. The error estimator for phase field is new since it can consider meshes which contain elements of arbitrary size and polynomial order. The arbitrary polynomial order will be shown to be particularly useful to reduce the required element size along the crack path leading to a reduction in computational time and the number of degrees of freedom. The error estimator can be used to determine the error for meshes which are heterogeneous in polynomial order and size, this means h and p-refinement can occur based on the smoothness of the solution field, leading to exponential convergence of the error with increasing DOF.

Numerical examples are used to show that hp-adaptivity significantly outperforms h-adaptive methods for the phase field solution in terms of the error value as a function of DOF. An hp *a posteriori* residual-based error estimator is also considered for the elasticity problem which is shown to be necessary for strongly coupled instantaneous crack propagation, and accurate fracture prediction in general. The hp-adaptive DG framework for the coupled problem is solved using a Light-Broyden–Fletcher–Goldfarb–Shanno quasi-Newton (L-BFGS) solver [39,43]. The BFGS method is used since it is relatively simple to implement as it only requires variations of the energy functional with respect to each primary variable separately. It has also been shown to achieve fast convergence compared to AM schemes. The combination of the BFGS solver with an hp-adaptive DG framework creates a method which is efficient in terms of both DOF and number of iterations to obtain a solution whilst being able to capture instantaneous fracture propagation. A key advantage of the proposed method is that it predicts accurate, self correcting, fracture propagation networks irrespective of the initial mesh and the user's knowledge of the expected fracture paths.

2. Phase field fracture

Phase field fracture models couple elasticity and a phase field that characterises the crack. Here the problem is solved in a two-dimensional polygonal domain $\Omega \subset \mathbb{R}^2$, whose boundary is given by $\partial \Omega \subset \mathbb{R}^2$. The strong form for elasticity is,

$$
\begin{aligned}
\nabla \cdot \boldsymbol{\sigma}(\boldsymbol{u}, \phi) &= \boldsymbol{0} & \text{in} & \quad \Omega \\
\boldsymbol{\sigma}(\boldsymbol{u}, \phi) \cdot \boldsymbol{n} &= \boldsymbol{g}_N^u & \text{on} & \quad \partial \Omega_N^u \\
\boldsymbol{u} &= \boldsymbol{g}_D^u & \text{on} & \quad \partial \Omega_D^u
\end{aligned}
\tag{1}
$$

where the superscript u denotes a function, or set, for the elasticity problem. In (1) $\boldsymbol{u} \in [H^1(\Omega)]^2$ is the displacement vector, following the hybrid phase field ideology of [59] the Cauchy stress tensor is defined as

$$
\boldsymbol{\sigma} = [(1 - \phi)^2 + \kappa]\boldsymbol{D} : \boldsymbol{\varepsilon} \quad \text{where} \quad \boldsymbol{\varepsilon}(\boldsymbol{u}) = \frac{1}{2} \left(\nabla \boldsymbol{u} + \nabla \boldsymbol{u}^T \right),
$$

$\boldsymbol{D}$ is the fourth order material tensor for elasticity, ϕ is the phase field and $0 < \kappa \ll 1$ is a stabilisation term [41]. Additionally $\boldsymbol{n} = (n_x, n_y)$ is the outward normal to $\partial \Omega$, and $\boldsymbol{g}_N^u \in [L^2(\partial \Omega_N^u)]^2$ and $\boldsymbol{g}_D^u \in [H^{1/2}(\partial \Omega_D^u)]^2$ are Neumann and Dirichlet boundary conditions, respectively. The union of the Neumann boundary, $\partial \Omega_N^u \subset \mathbb{R}^2$, and the Dirichlet boundary, $\partial \Omega_D^u \subset \mathbb{R}^2$, form the domain's boundary $\partial \Omega_N^u \cup \partial \Omega_D^u = \partial \Omega$, where $\partial \Omega_N^u \cap \partial \Omega_D^u = \emptyset$.

The strong form for the phase field, ϕ, can be expressed as

$$
\begin{aligned}
\left(\frac{G_c}{l} + 2\mathcal{H}(\boldsymbol{\varepsilon}) \right) \phi - G_c l \, \Delta \phi &= 2\mathcal{H}(\boldsymbol{\varepsilon}) & \text{in} & \quad \Omega \\
\nabla \phi \cdot \boldsymbol{n} &= g_N^\phi & \text{on} & \quad \partial \Omega_N^\phi \\
\phi &= g_D^\phi & \text{on} & \quad \partial \Omega_D^\phi
\end{aligned}
\tag{2}
$$

where l is the length scale, the superscript ϕ denotes a function or set for the phase field problem and $\mathcal{H}(\boldsymbol{\varepsilon}) \in [L^2(\Omega)]$ is the history field functional (explained below). $g_N^\phi \in L^2(\partial \Omega_N^\phi)$ and $g_D^\phi \in H^{1/2}(\partial \Omega_D^\phi)$ are respectively the Neumann and the Dirichlet boundary conditions on $\partial \Omega_N^\phi \subset \mathbb{R}^2$ and $\partial \Omega_D^\phi \subset \mathbb{R}^2$ where, $\partial \Omega_N^\phi \cup \partial \Omega_D^\phi = \partial \Omega$ and $\partial \Omega_N^\phi \cap \partial \Omega_D^\phi = \emptyset$. For all the problems considered here the boundary is only homogeneous Neumann ($g_N^\phi = 0$), however the functions g_N^ϕ and g_D^ϕ are provided here for completeness.

The phase field is coupled to the elastic displacement field through $\mathcal{H}$. In this paper, $\mathcal{H}$ is taken as the maximum positive strain energy density field $\psi^+(\varepsilon)$ over the set of the total time $t \in T \subset \mathbb{R}^+$, such that the history at a point is $\mathcal{H} = \max_{t \in T}(\psi_t^+(\varepsilon))$. The positive strain energy follows the decomposition of Miehe et al. [41] where $\psi^+(\varepsilon)$ is defined as

$$
\psi^+(\boldsymbol{\varepsilon}) = \frac{\lambda}{2} \langle \text{tr}(\boldsymbol{\varepsilon}^+) \rangle^2 + \mu \text{tr} \left(\boldsymbol{\varepsilon}^+ \cdot \boldsymbol{\varepsilon}^+ \right),
\tag{3}
$$

where $\boldsymbol{\varepsilon}^+$ is the tensile strain tensor

$$
\boldsymbol{\varepsilon}^+ = \sum_i^d \langle \varepsilon_i \rangle \boldsymbol{m}_i \boldsymbol{m}_i^\top
$$

d is the number of dimensions, i is the eigenvalue number, ε is the eigenvalue, $\boldsymbol{m}$ is the normalised eigenvector and $\langle \cdot \rangle = (|\cdot| + \cdot)/2$ denotes positive Macaulay brackets. Lastly, λ and μ are the Lamé parameters of the *undamaged* elastic solid, where the Young's modulus and Poisson's ratio are respectively defined as

$$
E = \frac{\mu(3\lambda + 2\mu)}{\lambda + \mu} \quad \text{and} \quad \nu = \frac{\lambda}{2(\lambda + \mu)}.
$$

3. Discontinuous Galerkin discretisation and error estimator

This paper uses error driven hp-adaptivity to achieve accurate solutions for the phase-field fracture with no *a priori* knowledge of the fracture path, or more generally where refinement is required throughout the domain to achieve an accurate solution. As discussed in the Introduction, both hp-CG and hp-DG have a range of advantages and disadvantages when considering meshes that contain elements of arbitrary size and polynomial order. The hp-CG method is already available in the literature with an error indicator for the phase-field [54]. A hp-DG scheme is

used here since it is perceived that it is algorithmically simpler to allow the face integral terms to naturally handle the hanging nodes and jumps in polynomial order. To solve the coupled problem using DG finite elements, the continuous polygonal domain Ω is subdivided by triangular elements K to form an unstructured mesh $\mathcal{T}$. Each element, K, has a polynomial order p_K with Lobatto basis functions [55]. The same discretisation is used for the elasticity and phase field equations. We also define the vector $p = \{\, p_K \,:\, K \in \mathcal{T}\,\}$ for elements in $\mathcal{T}$. The mesh will, in general, be heterogeneous in its polynomial order and will have hanging nodes. Each element $K \in \mathcal{T}$ has three edges. If there is an intersection between two elements, K^+ and K^-, then the interior edge $F = \partial K^+ \cap \partial K^-$ exists, the edge F then is in the set of all interior edges is $\mathcal{F}_I$. Additionally for the element K^+ and K^- their corresponding variables and functions are given the corresponding $+$ or $-$ superscript. If an edge ∂K^+, of K^+, does not intersect with another element then the edge exists on the boundary of the domain, i.e. $F = \partial K \cap \partial \Omega$. For problem (1), a face F along the boundary is either contained in $\mathcal{F}_D^u$ or $\mathcal{F}_N^u$, respectively the sets of edges forming the Dirichlet and Neumann portions of the boundary. Similarly, for problem (2), a face F along the boundary is either contained in $\mathcal{F}_D^\phi$ or $\mathcal{F}_N^\phi$. $\mathcal{F}$ is the set of all edges in the mesh. The functional space for the hp-Symmetric Interior Penalty (SIP) DG method is defined as $W_h = \{w \in L^2(\Omega) : \forall K, w|_K \in \mathcal{P}_{p_K}(K)\}$, where the elementwise approximation of $\boldsymbol{u}$ and ϕ are respectively defined as $\boldsymbol{u}_h \in [W_h]^2$ and $\phi_h \in W_h$.

For both the elasticity and phase field solutions a robust residual based hp *a posteriori* error estimator is defined to drive mesh adaptivity (see [36] for details of the elasticity error estimator). To ensure reliability and efficiency a constraint on the mesh is required: neighbouring elements can only have a difference of 1 in their polynomial order and only 1 hanging node can exist along an edge [36]. Here error estimators are defined for both the phase field and elasticity solutions separately and used to drive the hp adaptivity as the phase field evolves through the computational domain. The error estimators are also used as stopping criteria to determine when the solution provided by a mesh for the elasticity or phase field is sufficiently accurate.

3.1. Elasticity bilinear form and error estimator

The bilinear symmetric interior penalty (SIP) DG form for elasticity and the corresponding error estimator were initially presented, with full derivations, in [36], and are only stated here for readability. The bilinear form for the elasticity problem is now introduced as $a(\phi; \boldsymbol{u}_h, \boldsymbol{v}) = l(\boldsymbol{v})$, where $\boldsymbol{u}_h, \boldsymbol{v} \in [W_h]^2$ are the trial and test function

$$
\begin{aligned}
a(\phi; \boldsymbol{u}_h, \boldsymbol{v}) = &\sum_{K \in \mathcal{T}} \int_K \boldsymbol{\sigma}(\boldsymbol{u}_h, \phi_h) : \boldsymbol{\varepsilon}(\boldsymbol{v}) \mathrm{d}\boldsymbol{x} \\
&+ \sum_{F \in \mathcal{F}_I \cup \mathcal{F}_D^u} \int_F \left(-\{\boldsymbol{\sigma}(\boldsymbol{u}_h, \phi_h)\} : [\![\boldsymbol{v}]\!] - [\![\boldsymbol{u}_h]\!] : \{\boldsymbol{\sigma}(\boldsymbol{v}, \phi_h)\} + \frac{\beta p_F^2}{h_F} [\![\boldsymbol{u}_h]\!] : [\![\boldsymbol{v}]\!] \right) \mathrm{d}\boldsymbol{x}
\end{aligned}
\tag{4}
$$

and

$$
\begin{aligned}
l(\phi; \boldsymbol{v}) = &\sum_{F \in \mathcal{F}_N^u} \int_F \boldsymbol{g}_N^u \cdot \boldsymbol{v} \mathrm{d}\boldsymbol{x} \\
&+ \sum_{F \in \mathcal{F}_D^u} \int_F \left(-\boldsymbol{g}_D^u \cdot \boldsymbol{\sigma}(\boldsymbol{v}, \phi)^+ \cdot \boldsymbol{n}^+ + \frac{\beta p_F^2}{h_F} \boldsymbol{g}_D^u \cdot \boldsymbol{v} \right) \mathrm{d}\boldsymbol{x}.
\end{aligned}
\tag{5}
$$

where $\boldsymbol{n}^+$ is the normal vector to the boundary of element K^+. For an interior edge $F \in \mathcal{F}_I$ the notations for jumps and averages across element boundaries are defined as

$$
[\![\boldsymbol{u}]\!] = \boldsymbol{u}^+ \otimes \boldsymbol{n}^+ - \boldsymbol{u}^- \otimes \boldsymbol{n}^+ \quad \text{and} \quad \{\boldsymbol{\sigma}(\boldsymbol{v}, \phi)\} = \frac{1}{2} \left(\boldsymbol{\sigma}(\boldsymbol{v}, \phi)^+ + \boldsymbol{\sigma}(\boldsymbol{v}, \phi)^- \right),
\tag{6}
$$

where in tensor notation $\boldsymbol{a} \otimes \boldsymbol{b} := a_i b_j$, and for a boundary edge $F \in \mathcal{F}_I \setminus \mathcal{F}$ as

$$
[\![\boldsymbol{u}]\!] = \boldsymbol{u}^+ \otimes \boldsymbol{n}^+ \quad \text{and} \quad \{\boldsymbol{\sigma}(\boldsymbol{v}, \phi)\} = \boldsymbol{\sigma}(\boldsymbol{v}, \phi)^+.
\tag{7}
$$

The edge polynomial order, p_F, is described as

$$
p_F = \begin{cases} \max\left(p_K^+, p_K^-\right), & \text{if on the internal edges,} \quad F = \partial K^+ \cap \partial K^- \in \mathcal{F}_I(\mathcal{T}), \\ p_K^+, & \text{if on the external edges,} \quad F = \partial K^+ \cap \partial \Omega \in \mathcal{F}(\mathcal{T}) \setminus \mathcal{F}_I(\mathcal{T}), \end{cases}
\tag{8}
$$

where h_F is the length of the edge F, and β is the penalty parameter for SIP DG elasticity that is a function of the elasticity coefficients multiplied by a small number to ensure coercivity [60]. For this problem $\beta = 100E$, where E is the Young's modulus of the material. Normally a value of 10 is sufficient [7], however here 100 is used to reduce the DG solution space and thus help the convergence of the quasi-Newton solver. The error estimator for the elasticity problem is defined η_u with its full form provided in [36]. It can be shown that η_u is efficient and reliable for the true DG natural norm $\| \cdot \|_{\mathcal{T}}$ (also provided in [36]), that is

$$c_u \eta_u \leq \| \boldsymbol{u} - \boldsymbol{u}_h \|_{\mathcal{T}} \leq C_u \eta_u, \tag{9}$$

where c_u and C_u are constants independent of element size and polynomial order.

3.2. Phase field bilinear form

The bilinear SIP DG form for the phase field is $b(\mathcal{H}(\boldsymbol{\varepsilon}); \phi_h, \psi,) = I(\psi)$, where $\phi_h, \psi \in W_h$ is the trial and test function

$$
\begin{aligned}
b(\mathcal{H}(\boldsymbol{\varepsilon}); \phi_h, \psi,) &= \sum_{K \in \mathcal{T}} \int_K \left[\left(\frac{G_c}{l} + 2\mathcal{H}(\boldsymbol{\varepsilon}) \right) \psi \phi_h + G_c l \nabla \psi \cdot \nabla \phi_h \right] \mathrm{d}\boldsymbol{x} \\
&+ \sum_{F \in \mathscr{F}_I \cup \mathscr{F}_D^\phi} \int_F \left(-G_c l \{ \nabla \psi \} \cdot [\![\phi_h]\!] - G_c l [\![\psi]\!] \cdot \{ \nabla \phi_h \} + \frac{\gamma p_F^2}{h_F} [\![\psi]\!] \cdot [\![\phi_h]\!] \right) \mathrm{d}\boldsymbol{x}
\end{aligned}
\tag{10}
$$

and

$$
\begin{aligned}
I(\mathcal{H}(\boldsymbol{\varepsilon}); \psi) &= \sum_{K \in \mathcal{T}} \int_K 2\mathcal{H}(\boldsymbol{\varepsilon}) \psi \, \mathrm{d}\boldsymbol{x} + \sum_{F \in \mathscr{F}_N^\phi} \int_F g_N^\phi \psi \, \mathrm{d}\boldsymbol{x} \\
&+ \sum_{F \in \mathscr{F}_D^\phi} \int_F \left(-G_c l [\![g_D^\phi]\!] \cdot \{ \nabla \psi \} + \frac{\gamma p_F^2}{h_F} g_D^\phi \psi \right) \mathrm{d}\boldsymbol{x}.
\end{aligned}
\tag{11}
$$

The jumps and average operators across interior edges $F \in \mathscr{F}_I$ are

$$[\![\psi]\!] = \boldsymbol{n}^+ \psi^+ - \boldsymbol{n}^+ \psi^- \quad \text{and} \quad \{ \nabla \psi \} = \frac{1}{2} \left(\nabla \psi^+ + \nabla \psi^- \right), \tag{12}$$

and on the boundary edges, $F \in \mathscr{F}_I \setminus \mathscr{F}$

$$[\![\psi]\!] = \boldsymbol{n}^+ \psi^+ \quad \text{and} \quad \{ \nabla \psi \} = \nabla \psi^+. \tag{13}$$

p_F and h_F have the same form as for the elasticity problem. The form of the penalty parameter γ can be found through following the derivation for the SIP DG form in [60], and has the form $\gamma = 100 G_c l$. The penalty is a function of only the Laplacian coefficient in Eq. (2), to ensure coercivity, and thus the coefficients in the penalty, see [60].

3.3. Phase field error estimator

Here a robust hp-error estimator for phase-field fracture is defined. This error estimator for the phase-field has not yet been presented in the literature. It can be applied to hp-finite elements, is robust, and utilises the primary solution fields on the current mesh to compute the error. Therefore, no further systems of equations need to be solved. Both the elasticity and phase field problems are elliptic. The elasticity error estimator from [36] therefore provides a useful framework for the development of a phase field error estimator. There is however an additional reaction term, ϕ, in the phase field strong form (2), that also appears in the energy norm. Due to these similarities, and the derivation being beyond the scope of this paper, the error estimator is presented in a similar form to that in [36] and is shown numerically to be reliable and efficient for the true error up to some constants, in Section 7.1.

The error estimator for the phase field, η_ϕ, should provide a measure of the error in the energy norm of the DG phase field formulation, which is defined as

$$
\|\phi\|_\mathcal{T} := \left(\sum_{K \in \mathcal{T}} \|(G_c l)^{1/2} \nabla\phi\|_{0,K}^2 + \sum_{K \in \mathcal{T}} \|(G_c/l + 2\mathcal{H}(\boldsymbol{\varepsilon}))^{1/2}\phi\|_{0,K}^2 + \right.
$$
$$
\left. \sum_{F \in \mathcal{F}_I(\mathcal{T})} \frac{\gamma p_F^2}{h_F} \|[\![\phi]\!]\|_{0,F}^2 + \sum_{F \in \mathcal{F}_D^\phi(\mathcal{T})} \frac{\gamma p_F^2}{h_F} \|\phi\|_{0,F}^2 \right)^{1/2}
\tag{14}
$$

where $\|\cdot\|_{0,.}$ is the L^2 norm. For an error estimator to be useful it is necessary that it is never too far away from the true error in the natural norm, this is defined as the error estimator bounding the true error from below and above by some constants c_ϕ and C_ϕ, the constants c_ϕ and C_ϕ are independent of the element size, polynomial order and problem constants. The error estimator is respectively efficient and reliable

$$
c_\phi \eta_\phi \leq \|\phi - \phi_h\|_\mathcal{T} \leq C_\phi \eta_\phi.
\tag{15}
$$

Eq. (15) ensures as the error estimate convergences the true error will converge at a similar rate.

Similar to the elasticity error estimator [36], the global phase field error estimator η_ϕ is defined as

$$
\eta_\phi = \sqrt{\sum_{K \in \mathcal{T}} \left(\eta_{R,K}^2 + \eta_{J,K}^2 + \eta_{F,K}^2 \right)} = \sqrt{\sum_{K \in \mathcal{T}} \eta_{K,\phi}^2}
\tag{16}
$$

where a single element error estimate is

$$
\eta_{K,\phi}^2 = \eta_{R,K}^2 + \eta_{J,K}^2 + \eta_{F,K}^2.
\tag{17}
$$

This element error measure is also used to mark the elements with the highest errors for refinement. The first component of the element error estimator is an area integral defined as

$$
\eta_{R,K}^2 = \frac{h_K^2}{p_K^2 G_c l} \left\| \left(\frac{G_c}{l} + 2\mathcal{H} \right)\phi_h - G_c l \Delta\phi_h - 2\mathcal{H} \right\|_{0,K}^2,
\tag{18}
$$

where h_K is the inner diameter of element K. This term measures how well the strong form of the phase field equation (the first equation in (2)) has been satisfied by the weak finite element formulation.

As DG methods do not satisfy $\mathcal{C}^0$ continuity across elements, jumps in phase field exist between elements on the segment $F \in \mathcal{F}_I(\mathcal{T})$. As the Dirichlet boundary conditions are also imposed weakly, jumps in the phase field boundary condition will also exist between the phase field solution on the element boundary and the boundary condition imposed on them. Since the true solution for phase field should be continuous across these boundaries, the error in the jump in phase field on the edge $F \in \mathcal{F}_I(\mathcal{T})$ and the Dirichlet boundary $F \in \mathcal{F}_D(\mathcal{T})$ are measured as

$$
\eta_{J,K}^2 = \frac{1}{2} \sum_{F \in \mathcal{F}_I \cap \partial K} \frac{\gamma^2 p_F^3}{h_F G_c l} \left\| [\![\phi_h]\!] \right\|_{0,F}^2 + \sum_{F \in \mathcal{F}_D^\phi \cap \partial K} \frac{\gamma^2 p_F^3}{h_F G_c l} \left\| \left(\phi_h - \mathbf{g}_D^\phi \right) \right\|_{0,F}^2.
\tag{19}
$$

Like most finite element methods, SIP DG does not satisfy $\mathcal{C}^1$ continuity across the interior edges $F \in \mathcal{F}_I(\mathcal{T})$ and the Neumann boundary $F \in \mathcal{F}_N(\mathcal{T})$. These errors are estimated using

$$
\eta_{F,K}^2 = \frac{1}{2} \sum_{F \in \mathcal{F}_I \cap \partial K} \frac{h_F}{p_F G_c l} \left\| G_c l [\![\nabla\phi_h]\!] \right\|_{0,F}^2 + \sum_{F \in \mathcal{F}_N^\phi \cap \partial K} \frac{h_F}{p_F G_c l} \left\| G_c l \left(\nabla\phi \cdot \boldsymbol{n} - \mathbf{g}_N^\phi \right) \right\|_{0,F}^2.
\tag{20}
$$

The above terms allow the computation of an estimate of the error on each element in the finite element mesh. These errors can then be used to drive h and p adaptivity, as described in Section 5.

4. Incremental solution algorithm

The previous sections have provided the bilinear forms for the linear elastic and phase field problems. This section details the quasi-Newton method that is adopted to solve these coupled equations. Coupled phase field problems

typically require a high number of iterations per load step to arrive at a solution that reasonably satisfies both sets of equations [42]. This issue is compounded by any *hp*-adaptive scheme as it will be necessary to repeat load steps as the mesh is adapted. To mitigate some of these issues, a Broyden–Fletcher–Goldfarb–Shanno (BFGS) quasi-Newton method is selected to solve the coupled equations. This is motivated by the fact that the method has been shown to reduce the both the number of iterations per load step and the number of times the global stiffness matrix needs to be computed, both of which save on run-time [39]. Specifically, the Light-BFGS (L-BFGS) method is used since it strictly avoids the formation of large dense matrices [61]. Here, similar to [43], a line search is used to prevent the solution during a load step from diverging. Additionally, if the load step is too large the solution to the non-linear problem can be too far away for the solver to find a solution, hence the adaptive load-step method from [39] is used to reduce the load step size during significant fracture development. This also improves the accuracy of reaction force with displacement curves.

4.1. L-BFGS (Light - Broyden–Fletcher–Goldfarb–Shanno) quasi-Newton solver

In order to solve the non-linear problem using a quasi-Newton method, the bilinear forms in Sections 3.1 and 3.2 need to be linearised with respect to their trial functions. When linearising the bilinear forms the coupling terms are assumed constant, that is, for elasticity ϕ_h is constant with respect to $\boldsymbol{u}_h$, and for the phase field $\mathcal{H}$ is constant with respect to ϕ_h. The linearised bilinear form for elasticity about the solution $\bar{\boldsymbol{u}}$ is therefore

$$L^u(\phi_h; \delta\boldsymbol{u}_h, \bar{\boldsymbol{u}}_h) = r_h^u(\phi_h; \bar{\boldsymbol{u}}_h, \boldsymbol{v}) + Dq^u(\phi_h; \bar{\boldsymbol{u}}_h, \boldsymbol{v})[\delta\boldsymbol{u}_h] = 0 \tag{21}$$

and for the phase field about the solution $\bar{\phi}_h$ is

$$L^\phi(\mathcal{H}; \delta\phi_h, \bar{\phi}_h) = r_h^\phi(\mathcal{H}; \bar{\phi}_h, \psi) + Dq^\phi(\mathcal{H}; \bar{\phi}_h, \psi)[\delta\phi_h] = 0 \tag{22}$$

where the residuals are $r_h^u(\phi_h; \bar{\boldsymbol{u}}_h, \boldsymbol{v}) = a(\phi_h; \bar{\boldsymbol{u}}_h, \boldsymbol{v}) - l(\phi; \boldsymbol{v})$ and $r_h^\phi(\mathcal{H}, \bar{\phi}_h, \psi) = b(\mathcal{H}; \bar{\phi}_h, \psi) - I(\mathcal{H}; \psi)$. $Dr_h^u(\phi_h; \bar{\boldsymbol{u}}_h, \boldsymbol{v})[\delta\boldsymbol{u}_h]$ and $Dq^\phi(\mathcal{H}; \bar{\phi}_h, \psi)[\delta\phi_h]$ are the directional derivatives of $r_h^u(\phi_h; \bar{\boldsymbol{u}}_h, \boldsymbol{v})$ and $r_h^\phi(\mathcal{H}, \bar{\phi}_h, \psi)$ in the directions $[\delta\boldsymbol{u}_h]$ and $[\delta\phi_h]$ at $\bar{\boldsymbol{u}}_h$ and $\bar{\phi}_h$ respectively. The directional derivatives for the elasticity and phase field problems are

$$Dq^u(\phi_h; \bar{\boldsymbol{u}}_h, \boldsymbol{v})[\delta\boldsymbol{u}_h] = \sum_{K\in\mathcal{T}} \int_K \boldsymbol{\sigma}(\delta\boldsymbol{u}_h, \phi_h) : \boldsymbol{\varepsilon}(\boldsymbol{v})\mathrm{d}\boldsymbol{x}$$
$$+ \sum_{F\in\mathscr{F}_I\cup\mathscr{F}_D} \int_F \left(-\{\boldsymbol{\sigma}(\delta\boldsymbol{u}_h, \phi_h)\} : [\![\boldsymbol{v}]\!] - [\![\delta\boldsymbol{u}_h]\!] : \{\boldsymbol{\sigma}(\boldsymbol{v}, \phi_h)\} + \frac{\beta p_K^2}{h_K}[\![\delta\boldsymbol{u}_h]\!] : [\![\boldsymbol{v}]\!] \right) \mathrm{d}\boldsymbol{x} \tag{23}$$

and

$$Dq^\phi(\mathcal{H}; \bar{\phi}_h, \psi)[\delta\phi_h] = \sum_{K\in\mathcal{T}} \int_K \left[\left(\frac{G_c}{l} + 2\mathcal{H} \right) \psi\delta\phi_h + G_c l\nabla\psi \cdot \nabla\delta\phi_h \right]\mathrm{d}\boldsymbol{x}$$
$$+ \sum_{F\in\mathscr{F}_I\cup\mathscr{F}_D} \int_F \left(-G_c l\{\nabla\psi\} \cdot [\![\delta\phi_h]\!] - G_c l[\![\psi]\!] \cdot \{\nabla\delta\phi\} + \frac{\gamma p_F^2}{h_F}[\![\psi]\!] \cdot [\![\delta\phi_h]\!] \right)\mathrm{d}\boldsymbol{x}. \tag{24}$$

To solve the linearised systems of equations using finite elements, the polynomial basis and corresponding coefficients are substituted into Eqs. (21) and (22) for all the test and trial functions, to obtain

$$\{r_h^u\} = -[K_{uu}]\{\delta u_h\} \quad \text{and} \quad \{r_h^\phi\} = -[K_{\phi\phi}]\{\delta\phi_h\} \tag{25}$$

where the subscript h denotes the finite element approximation, $\{\cdot\}$ is a vector where the rows correspond to DOF numbers, $[\cdot]$ is a matrix where the rows and columns both refer to DOF numbers, and $[K_{uu}]$ and $[K_{\phi\phi}]$ are the tangent matrices for the two equations. The complete linear system of equations, with the subscript h dropped for readability, is written as

$$\begin{Bmatrix} \{r^u\} \\ \{r^\phi\} \end{Bmatrix}^n = - \begin{bmatrix} [K_{uu}] & 0 \\ 0 & [K_{\phi\phi}] \end{bmatrix}^n \begin{Bmatrix} \{\delta u\} \\ \{\delta\phi\} \end{Bmatrix}^{n+1}, \tag{26}$$

where n is the iteration step number, $\{\delta\cdot\} = (\{\cdot\}^{n+1} - \{\cdot\}^n)$. The linearised system can subsequently be condensed down to

$$\{r\}^n = -[K_0]\{z\}^{n+1}, \tag{27}$$

where the form of the linearised system of Eqs. (27) is the robust alternate minimisation (AM) form for solving the phase field fracture problem for a load increment [2].

The L-BFGS method uses an approximation of the problem's Hessian $[\tilde{K}]$ to solve the problem,

$$\{r\}^n = -[\tilde{K}_n]\{z\}^{n+1}, \tag{28}$$

but instead of computing the Hessian exactly it is updated using the secant equation,

$$[\tilde{K}_{n+1}] = [\tilde{K}_n] - \frac{([\tilde{K}_n]\{z\})([\tilde{K}_n]\{z\})^\top}{\{z\}^\top[\tilde{K}_n]\{z\}} + \frac{\{\Delta r\}\{\Delta r\}^\top}{\{z\}^\top\{\Delta r\}}. \tag{29}$$

with the change in residual $\{\Delta r\} = \{r\}^{n+1} - \{r\}^n$, solution $\{z\}$ and previously approximated Hessian $[\tilde{K}_n]$. For the first solve the uncoupled matrix is used $[\tilde{K}_1] = [K_0]$.

In this paper the L-BFGS algorithm is employed in the computation of $[\tilde{K}_n]$, this is because the update of the $[\tilde{K}_n]$ in (29) will produce a dense matrix which becomes very memory intensive for any reasonably sized finite element problem. To solve (28) without computing $[\tilde{K}_n]$ the *two loop recursion* algorithm for the L-BFGS method is employed, which exploits the recursive natural of the secant matrix update, (29), to solve Eq. (28). The algorithm is explained in full in [61] and is provided here with Algorithm 1 using notation consistent with [61], where

$$\{u\phi\}^\top = \{\{u\}^\top\{\phi\}^\top\}.$$

and the remaining ρ_i, a_i and $\{q\}$ are temporary storage variables with their mathematical definition provided in [61].

Algorithm 1: L-BFGS algorithm solving for $\{z\}^{n+1}$

$\{q\} \leftarrow \{r\}_{n-1}$;
for $i = (n-1) : -1 : 1$ **do**
  $\rho_i = 1/(\{\{u\phi\}_{i+1} - \{u\phi\}_i\}^\top\{r_{i+1} - r_i\})$;
  $a_i = \rho_i\{\{u\phi\}_{i+1} - \{u\phi\}_i\}^\top q$;
  $\{q\} = \{q\} - a_i\{\{r\}_{i+1} - \{r\}_i\}$;
end
$\{z\} = [K_0]^{-1}\{q\}$;
for $i = 1 : 1 : (n-1)$ **do**
  $\beta_i = \rho_i\{\{r\}_{i+1} - \{r\}_i\}^\top\{z\}$;
  $\{z\} = \{z\} + \{\{u\phi\}_{i+1} - \{u\phi\}_i\}(a_i - \beta_i)$;
end
$\{z\} = -\{z\}$;

The update avoids the use of dense matrices by storing n times the residual and solution. To prevent floating point numerical errors in the update of approximate Hessian matrix, the number of secant matrix updates, n, is set as $n_{limit} = 10$, [43]. Once this limit is reached the matrix $[K_0]$ is recomputed using the current solution, Eq. (26), and the solution variables, residual and increment number are reset: $\{u_{n+1}\} \rightarrow \{u_1\}$; $\{\phi_{n+1}\} \rightarrow \{\phi_1\}$; $\{r_{n+1}\} \rightarrow \{r_1\}$; and $n = 1$.

4.2. Line search

A quasi-Newton method is typically globally convergent when accompanied by a line search [43,62]. However, in the case of the BFGS method with phase field fracture, Kristensen et al. [39] found that line searches may not be necessary. However when a poor mesh was used, which was often the case with adaptivity, and no line search was employed, the L-BFGS method was found often to diverge. To prevent this, an energy minimisation line search is used [40],[1] but only called when the problem is considered to be diverging, which was determined by a suitably high residual value of $|\{r\}| > 10^{-2}$. While it is generally more robust to perform a line search each iteration, a limit on the residual value was found to be sufficient.

---

[1] Other more robust methods for determine the step size exist, such as the Wolfe line search, which also considers the updated residual [62].

When a line search is used, a scaling factor $s_f \in (0, 1]$ is applied to the update, determined using a backward line search algorithm based on energy minimisation [40]. The line search employed here is coarse, limited to $s_f \in A = \{0.5, 0.01, 0.001\}$, and simply written as

$$s_f = \underset{s_f \in A}{\arg \min} \; En(s_f, z, U_n),$$

where En is the total energy of the system [40].

4.3. Adaptive load stepping

The algorithm for step adaptivity from [39] is used to determine if the load step, Δg_D^u, is too large and thus too far away for the solver to find a solution. When this is the case the load step, $|\Delta g_D^u|$, needs to be decreased and the solution algorithm restarted. Therefore in order to enable large load steps when the solution is only slightly non-linear, and small load steps to ensure convergence when the solution is highly non-linear, the simple and robust adaptive load step algorithm from [39] is employed and is detailed in Algorithm 2. The algorithm loops over all integration points in the mesh for current iteration n. If an integration point i undergoes a large jump in phase field value, $\Delta \phi_i \geq 0.5$, and its previous value was relatively low, $\phi_i^{n-1} < 0.7$, the step size is reduced by a factor of 10. To prevent continuous reductions in the step size during instantaneous crack propagation, the load increment is only allowed to decrease once during the load step and reset to the maximum value at the beginning of the next step.

Algorithm 2: Rerun check

For any integration point i;
if $\phi_i^{n-1} < 0.7$ *AND* $\Delta \phi_i \geq 0.5$ **then**
    | Rerun load increment and set $\Delta g_D^u \leftarrow 0.1 \Delta g_D^u$.;
end

4.4. Single increment solution algorithm

In the preceding sections the components for the incremental solution algorithm were provided, in this section they are combined into Algorithm 3 which can be divided into several three key sections:

1. Using the history field from the previous converged solution, $\mathcal{H}$, obtain $\{\phi\}^1$ and subsequently $\{u\}^1$ by performing a linear solve. Compute the corresponding residual $\{r\}^1$.
2. Enter the first while loop and determine the first update to the solution, compute the matrix $[K_0]$, using $\{\phi\}_1$ and $\{u\}_1$, as the first approximation to the Hessian $[\tilde{K}]$; and
3. A system of nested while loops is employed, inside which the L-BFGS algorithm is used along with a series of exit conditions for the main, and nested, while loops.

The exit conditions are an important aspect of the solver since they control when the L-BFGS solver has to be reset and when the load increment size needs to be reduced. They also flag when to stop the algorithm once a sufficient tolerance in the residual is reached or the step size, Δg_D^u, needs to be reduced. The exit condition to reset the L-BFGS solver is initiated when the iteration count, n, for the L-BFGS solver reaches its limit n_{limit}.

5. Adaptivity

There are several motivators for using mesh adaptivity when modelling a phase field fracture problem, specifically: (i) adaptivity provides a means to obtain an accurate representation of the stress field and associated fracture growth; (ii) adaptivity is efficient in terms of the number of DOF required to solve the problem in that hp refinement is performed only where necessary to obtain a solution to a desired accuracy; and (iii) adaptivity removes the requirement to know *a priori* how the solution will evolve. This allows non-trivial problems to be solved with

---

Algorithm 3: Solution for current load step i

Use the staggered scheme to solve for $\{\phi\}^1$ and $\{u\}^1$ using the previous converged history field $\mathcal{H}^{i-1}$ and total load $\Delta \boldsymbol{g}_D^{u,i-1}$;

Set the Dirichlet boundary condition for elasticity as $\boldsymbol{g}_D^{u,i} = \boldsymbol{g}_D^{u,i-1} + \Delta \boldsymbol{g}_D^{u,i}$;

while *main exit flag is false* **do**

    Set $n = 1$, and sub loop exit flag to false;

    Compute $[K_0]$;

    while *sub loop exit flag is false* **do**

        $\{z\}^{n+1} \leftarrow$ from Algorithm 1;

        $\{u\phi\}^{n+1} = \{u\phi\}^n + \{z\}^{n+1}$;

        Compute the history field $\mathcal{H}$ and subsequently $\{r\}^{n+1}$;

        if $\|\{r\}^{n+1}\|_0 > 10^{-2}$ & $n > 2$ **then**

            $s_f = \arg\min_{s_f \in A} En(a, z, U_n)$;

            $\{u\phi\}^{n+1} = \{u\phi\}^n + s_f\{z\}^{n+1}$;

            Recompute the history field $\mathcal{H}$ and $\{r\}^{n+1}$;

        end

        if $n > 2$ **then**

            if $\Delta \boldsymbol{g}_D^{u,i}$ *larger than minimum its value AND* $(\|\{r\}^{n+1}\|_0 > tol)$ **then**

                Check Algorithm 2, if step size reduced set all exit flags to true.;

            end

            if $(\|\{r\}^{n+1}\|_0 < tol)$ **then**

                set all exit flags to true;

            else if $n \geq n_{limit}$ **then**

                set sub loop exit flag to true;

                $\{u\phi\}^1 \leftarrow \{u\phi\}^{n+1}$;

            end

        end

        $n = n + 1$;

    end

end

return $\{u\}, \{\phi\} \leftarrow \{u\phi\}^n$ and $\mathcal{H}$;

---

minimal initial input, compared to significant computational power required through global refinement of the finite element mesh.

For efficiency, *p*-refinement should only be performed in smooth parts of the solution, and *h* in nonsmooth regions [58]. Therefore in order to achieve the maximum decrease in the global error with minimal increases in the number of DOF, the elements with the highest error need to be identified as well as an estimate of their solution smoothness.

The algorithms in this paper assume triangular elements but the methods can be applied to other elements. When a triangular element is refined in *h* it is refined homogeneously, as in Fig. 1. The parent element, K, is split into four new child triangle elements $\{K_1, K_2, K_3, K_3\}$, all of which are similar to their parent. Each child will have polynomial order of their parent minus one, e.g. $p_{K_1} = p_K - 1$ for child K_1. Additionally a projection of the history field from the parent to the child elements is required (see Section 5.2).

5.1. Adaptive strategy

The adaptive strategy is controlled by the error estimators for the phase field and elasticity problem. Adaptivity occurs if either error estimate, η_u or η_ϕ, Eq. (16), is greater than their respective user defined tolerances, TOL_u and TOL_ϕ, Bird et al. [36]. An error estimate for a field is only used to mark elements for refinement if its corresponding
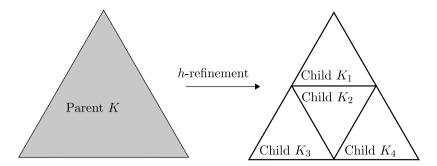
Fig. 1. Homogeneous h-refinement.

value is greater than a tolerance. Additionally there is a limit on the minimum size and maximum polynomial order of the elements, therefore when computing the errors

$$\eta_\phi = \sqrt{\sum_{K \in \mathcal{T}_{R,\phi}} \eta_{K,\phi}^2} \quad \text{and} \quad \eta_u = \sqrt{\sum_{K \in \mathcal{T}_{R,u}} \eta_{K,u}^2} \tag{30}$$

the subsets $\mathcal{T}_{R,\phi} \subset \mathcal{T}$ and $\mathcal{T}_{R,u} \subset \mathcal{T}$ are used, with $\eta_{K,u}^2$ defined in [36]. The subsets are determined by inspecting the smoothness, size and polynomial orders of an element. For the element K, if for a field the solution is smooth and K is of maximum polynomial order, $p_K = p_{max}$, or if it is not smooth and of minimum size, $h < h_{min}$, it is not in the set $\mathcal{T}_{R,\cdot}$ since it cannot be refined further. The smoothness of an element is found by projecting its solution to an orthogonal triangular basis of the same polynomial order [58]. If the coefficients of the basis decays exponentially with increasing polynomial order the element is considered smooth, otherwise it is non-smooth. The definition of the orthogonal basis, projection and proof for smoothness identification can all be found in [58].

The elements are marked based on a mean criteria [58], if an element's error is greater than the mean error for the respective field, multiplied by a factor R, then it is marked for refinement. The logic statement for an element to be refined is

$$[(\eta_{K,\phi}^2 > R\bar{\eta}_\phi)\text{AND}(\eta_\phi > TOL_\phi)]\text{OR}[(\eta_{K,u}^2 > R\bar{\eta}_u)\text{AND}(\eta_u > TOL_u)] \tag{31}$$

where the averages $\bar{\eta}_u$ and $\bar{\eta}_\phi$ are respectively

$$\bar{\eta}_\phi = \sum_{K \in \mathcal{T}_{R,phi}} \eta_{K,\phi}^2 / |\mathcal{T}_{R,phi}| \quad \text{and} \quad \bar{\eta}_u = \sum_{K \in \mathcal{T}_{R,u}} \eta_{K,u}^2 / |\mathcal{T}_{R,u}|.$$

If an element is marked for both h and p, it is refined in h to ensure that both errors will decrease for this element. The adaptive strategy is called if one of the error estimates is not below its tolerance. With these premises the adaptivity strategy can be defined,

1. For both $\boldsymbol{u}$ and ϕ solutions determine whether the solution space within each element is smooth or nonsmooth using the method presented in [58];
2. Determine the subsets $\mathcal{T}_{R,\phi} \subset \mathcal{T}$ and $\mathcal{T}_{R,u} \subset \mathcal{T}$;
3. Compute the η_ϕ and η_u using the summation definitions in (30);
4. If $\eta_u > TOL_u$ or $\eta_\phi > TOL_\phi$ then the mesh is refined;
5. Use (31) to mark elements for refinement;
6. Mark additional elements for refinement to ensure only 1 hanging node per face and a polynomial order difference of 1 between neighbouring elements (mesh smoothing step); and
7. Finally refine to get the new mesh $\mathcal{T}$.

5.2. History projection

The history functional is the only solution dependent property that has to be mapped between different meshes; all other material properties are uniform across the mesh. The mapping occurs each time an element is refined in

either h or p. When an element is refined in p the mapping is relatively simple since the domain of the element K remains unchanged. However, when the element is h-refined, K is divided into four child elements, K_c where $c \in [1, 4]$, where the union of the childrens' domains forms the parent's domain, see Fig. 1.

The history function is assumed to at best $\mathcal{H} \in L^2(K)$ with an additional constraint of always being greater than 0. Hence a nearest neighbour mapping is used to always ensure values greater than 0. The mapping occurs at the Gauss point level, where the location of a child's Gauss point is $\boldsymbol{x}_{n,c} \in K_c \cap K$, where $n \in N$ is the Gauss point number and N is the set of all Gauss point numbers in K_c. $\boldsymbol{x}_{n,c}$ takes the value equal to the value of the nearest parent Gauss point $\hat{\boldsymbol{x}}_m \in K$, where $m \in M$ is the Gauss point number and M is the set of all Gauss points numbers in K. For Gauss point n, the history is assigned as,

$$\mathcal{H}(\boldsymbol{x}_{n,c}) = \mathcal{H}(\boldsymbol{x}_m) \quad \text{where} \quad m = \arg\min_{m \in M}(|\boldsymbol{x}_{n,c} - \boldsymbol{x}_m|). \tag{32}$$

6. Complete fracture algorithm

The previous two sections have described the algorithms for determining the incremental solution and adapting the mesh. In this section the algorithms are combined to form Algorithm 4, for the complete fracture problem for a total boundary displacement of $\boldsymbol{g}_{D,\max}^u$. The algorithm is controlled by a pair of nested while loops. The outer loop checks whether the current load displacement $\boldsymbol{g}_{D,i}^u$ is greater than the maximum load displacement $\boldsymbol{g}_{D,\max}^u$. If not the nested while loop is called which solves for the current increment i. The L-BFGS method is used to solve for the current load $\boldsymbol{g}_{D,i+1} = \boldsymbol{g}_{D,i} + \Delta \boldsymbol{g}_{D,i}$ using Algorithm 3. If the solution is found the algorithm exits. Alternatively, either the step size, $\Delta \boldsymbol{g}_{D,i}$, is too big and needs to be reduced, or, the mesh needs to be refined.

Algorithm 4: main algorithm

Create mesh $\mathcal{T}$;
Set load step counter $i = 1$;
while $\boldsymbol{g}_{D,i}^u < \boldsymbol{g}_{D,\max}^u$ **do**
    reset $\Delta \boldsymbol{g}_{D,i}^u$ to its maximum value (Section 4.3);
    while $\eta_u > TOL_u$ AND $\eta_\phi > TOL_\phi$ **do**
        Compute the solution $\{u\}$, $\{\phi\}$ and $\mathcal{H}'$ using, Algorithm 3 and $\mathcal{H}$.;
        Determine the error estimates η_ϕ and η_u (see Eq. (30));
        Check restart condition;
        if *adaptive load step size is required (Section 4.3)* **then**
            $\Delta \boldsymbol{g}_{D,i} \leftarrow \Delta \boldsymbol{g}_{D,i}/10$;
        else
            if $\eta_u < TOL_u$ AND $\eta_\phi < TOL_\phi$ **then**
                $\boldsymbol{g}_{D,i+1} = \boldsymbol{g}_{D,i} + \Delta \boldsymbol{g}_{D,i}$;
                Store converged history solution $\mathcal{H} = \mathcal{H}'$ (Section 5.2);
                $i = i + 1$;
            else
                Define the history field as $\bar{\mathcal{H}}$;
                Refine the mesh to get the new mesh $\mathcal{T}$ (Section 5.1);
                Using a nearest point projection get $\mathcal{H} \leftarrow \tilde{\mathcal{H}}$ (Section 5.2);
            end
        end
    end
end

If the increment is too large, the load step is reduced, and Algorithm 3 is reattempted. If the solution is found the errors for both fields are checked. If they are sufficiently low the total load step is updated, the history field is stored and i is incremented. However, if either error is too large the history field for the current mesh is stored, the mesh is refined (see Section 5.1) to get the new mesh $\mathcal{T}$ and the new history field is projected onto the elements in the new mesh. Since the errors are too high the increment load step is reattempted, this loop will continue until the errors η_u and η_ϕ are less than their respective tolerances. The last condition is the check *check restart condition*,

this condition restarts the algorithm and only occurs once, resetting all values apart from the mesh data when the phase field reaches a value of 1 in the solution. This is necessary since when the algorithm first starts the mesh is poor, refinement on the boundary therefore causes large oscillations in the recorded load with applied displacement.

7. Numerical examples

Now that the *hp*-adaptive DG framework for phase field fracture, and the solution method, have been presented, it is necessary to show its efficiency and accuracy in solving a range of benchmark problems. Each benchmark problem will test a different aspect of the method and demonstrate its ability to solve a range of problems accurately. Four problems are considered:

1. Error estimator verification: to demonstrate the reliability and efficiency of the phase field error estimator, confirming that the error estimator provides a meaningful representation of the true error with *h* and *hp*-adaptive refinement for both boundary condition- and history field-driven problems.[2]
2. Single crack mode-I uniaxial tension test [41]: to demonstrate the ability of the proposed method to predict accurate mode-I fracture propagation starting from a very coarse initial mesh; and to the quantify the impact of the model parameters on the obtained results.
3. Single crack subjected to shear load: to demonstrate the ability of the proposed method to capture the correct fracture propagation path for starting from a very coarse initial mesh; and to highlight the importance of including error estimation for both the phase field and the linear-elasticity solutions.
4. Double crack uniaxial tension test: to demonstrate the ability of the method to represent multiple interacting cracks with adaptive mesh refinement whilst maintaining symmetry of the physical problem; and to highlight the importance of phase field and elasticity-driven mesh refinement.

The first test is to demonstrate reliability and efficiency. The method of manufactured solutions (MMS) is used to create an analytical solution for a phase field problem. The MMS is compared against the numerical solution which allows the true error in the DG norm to be calculated and compared with the error estimate. The remaining tests examine the phase field fracture problem. Each problem showcases the method's ability to solve a variety of problems. The solution to problem 2 is an approximately instantaneous crack propagation [39], in that total failure of the specimen occurs over a single load step. Problem 3 is shear loaded and has a more complicated response, comprising instantaneous crack propagation and gradual propagation with gradual load increase. This problem demonstrates that this more complicated response can be captured by the proposed approach. Problem 4 involves the interaction, and instantaneous propagation, of two cracks, making this a particularly difficult problem to model with mesh adaptivity, since the mesh both determines the interaction of the stress field between the two cracks and also influences where the cracks will propagate. This example will demonstrate the robustness of the residual *a posteriori* error estimate-based adaptive method.

Alongside the demonstration of the method's ability to model a range of propagation problems with different characteristics, the parameters which control mesh adaptivity and the limits on the smallest element size will be explored. The solution field of the phase field problem and the load–displacement response are examined and compared to benchmark results in the literature. The parameters that will be varied are: the minimum allowable element size, $h_{\min}$, the linear elastic error estimate threshold, and the phase field error estimate threshold.

For all numerical examples the Young's modulus, $E = 210$ GPa, the Poisson's ratio, $\nu = 0.3$, and the Griffith failure energy is $G_c = 2700$ N/m; the phase field length value l is varied between numerical simulations. The parameter R, which determines the proportion of elements to be refined, based on the average value as discussed in Section 5, is set at 0.5. As discussed by [58], to accurately determine whether an element should be refined in h or p using the smoothness criteria the element needs a polynomial order of at least 3, therefore for all meshes $p_K \ \forall K = 3$. The maximum polynomial order that an element can have is set to 6, it was generally observed that this polynomial order was sufficiently high to have large elements compared to the phase field length scale whilst also obtaining accurate results.

---

[2] Note that the reliability and efficiency of the linear elasticity error estimate is demonstrated by [36,63] and is therefore not repeated here.
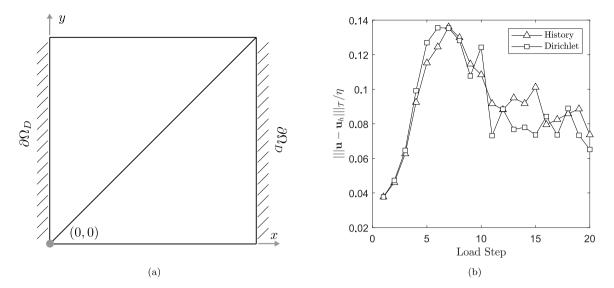
Fig. 2. Verification: (a) Initial mesh and boundary conditions and (b) error efficiency.

7.1. Problem 1, error estimator verification

Section 3.3 presented the error estimator for the phase field problem. This section will show numerically that the phase field error estimator bounds the true error in the energy norm from above and below up to some arbitrary constants independent of element polynomial order and size. It will also show the estimator to be an effective method to identify elements for hp-refinement achieving exponential convergence in the true error for the phase-field. In this section two problems are considered over the same unit domain, initial meshes, hp-adaptive scheme and using the same parameters. Only the phase field equations are solved for the problems in this section. The assumed solution to the problems are:

$$\begin{aligned} d &= e^{-x/l} &&: &&\text{Dirichlet analysis} \\ d &= e^{-75x} &&: &&\text{History analysis} \end{aligned} \tag{33}$$

where $l = 0.01$ and the applied history field and, Dirichlet and Neumann boundary conditions, are determined with the method of manufactured solutions. The first problem is the 1D solution to the phase field problem and in the numerical simulation a Dirichlet boundary condition of $d = 1$ is weakly imposed at $x = 0$ [3]. This problem will test the ability of the error estimator and the hp-adaptive method to efficiently refine to capture phase field distributions that represent a regularised crack geometry, however since the phase field is driven by a boundary condition rather than a history field the second problem is needed to fully verify the DG solver. The second problem is driven by the history field, and is used to show that error estimator is reliable and efficient for problems where the history field is non-zero. For both solutions the smoothness of the solution increases as x increases, hence near $x = 0$ it is expected that the solution will be sufficiently non-smooth to require hp-refinement, and away from $x = 0$ mostly only p-refinement will occur.

The domain is defined as $\Omega \in [0, 1]^2$ with $\partial \Omega = \partial \Omega_D \cup \partial \Omega_N$, and the domain and corresponding initial mesh for both problems is shown in Fig. 2(a). The variation of the ratio between the true and estimated error with hp-refinement step is shown in Fig. 2(b). Fig. 2(b) shows numerically that η_ϕ is efficient for the true error, this is shown by the oscillations in the ratio which are similar to those observed in [36]; this demonstrates η_ϕ can reliably be used as an accuracy threshold for the phase field solution.

The convergence of the true and estimated errors with the square root of the number of DOF (NDOF) for both problems with hp- and h-adaptivity is shown in Fig. 3. Fig. 3 shows that only with hp-adaptivity is continued exponential convergence achieved whilst h-adaptivity plateaus with increasing NDOF. This means that an error threshold is more attainable, with fewer DOF, with hp adaptivity compared to h-adaptivity in which it becomes
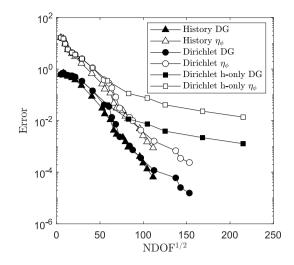
Fig. 3. Verification: convergence of the error estimate and the error in the DG norm, where η_ϕ is the phase field error estimator. The final log–log convergence rate on this log-linear plot (estimated with the last 3 points) using hp-adaptivity is 9.7, *History*, and 9.6, *Dirichlet*, for h-adaptivity the convergence is 2.02, *Dirichlet*.
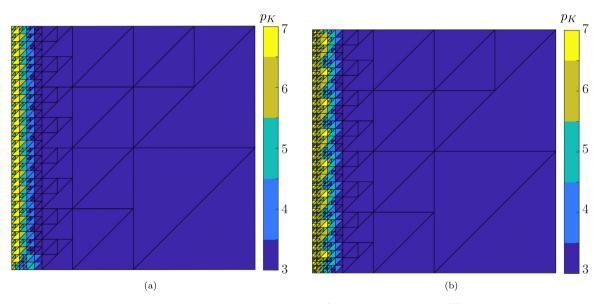

Fig. 4. Verification: final meshes for (a) Dirichlet- $(d = e^{-x/l})$ and (b) history- $(d = e^{-100x})$ driven problems.

computationally onerous to achieve the same error. The final mesh distributions for the Dirichlet-driven and history-driven hp-adaptive solutions are shown in Figs. 4(a) and 4(b), respectively. The elements with the highest error have automatically been identified by the error estimate, causing significant hp-refinement to occur near $x = 0$.

The final aspect to investigate is how the error is distributed through the domain, and whether it is actually worthwhile to consider high order elements to reduce the error in the phase field solution, particularly near the crack where the solution is the least smooth. To do this a comparison is made between the 1D fracture solution, $d = e^{-|x|/l}$, when using hp- and h-refinement schemes. The meshes used to generate the smallest error in Fig. 3 for the respective adaptivity schemes are used for the comparison. This corresponds to the hp-mesh provided in Fig. 4(a) and the h-refined mesh shown in Fig. 5(a) where $p_K = 3 \ \forall \ K$. For the h-adapted mesh in Fig. 5(a), the smallest elements are located near $x = 0$ with side lengths of 2^{-9} m, whereas the hp-adapted mesh has elements with side lengths 2^{-7}. Additionally, the distributed error in Fig. 5(b) shows that despite the elements being 4 times
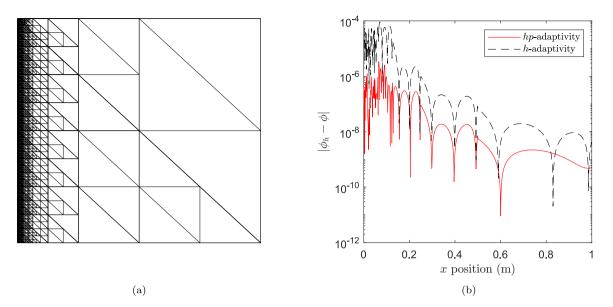
Fig. 5. Verification: final meshes for (a) h-adaptivity Dirichlet- ($d = e^{-x/l}$) and (b) a comparison of the phase-field error distribution along the line $(x, y) = [0, 1] \times [0.5]$ for the hp- and h-adaptive schemes.

larger at the least smooth region, $x = 0$, the error is consistently 1-to-2 orders of magnitude smaller for hp-refined mesh, which has elements of order 6 and 7 at the 1D crack. The global benefit of including p-adaptivity is also demonstrated in Fig. 3, where smaller errors for the hp-adaptivity are computed for fewer DOFs.

7.2. Problem 2, mode I edge crack

The mode-I crack problem is the *de facto* benchmark problem in the literature for instantaneous fracture propagation, [3]. The problem is difficult to solve with traditional fully-coupled Newton solvers as nearly all the phase field development occurs in one step, however the work of [40] details a Newton solver with positive and negative line search direction. The other alternative is solving with the AM algorithm, which is expensive due to the high iteration number and computation of the stiffness matrix at ach iteration [42].

This problem investigates how the accuracy of the fracture problem is influenced by the tolerance values for η_u and η_ϕ and the minimum element size. Controlling the minimum element size will demonstrate that high order elements reduce the requirement for small elements about the phase field fracture. As shown in Fig. 3, convergence of the phase field error with hp-adaptivity is exponential, suggesting that fewer DOF are required to achieved the same accuracy compared to the non-exponential h-adaptivity. This potentially indicates that the high polynomial order is reducing the need for very small elements around the phase field-represented fractures. The parameters that were varied over the five numerical experiments with their values are given in Table 1. The experiments are referred to by letter to improve the reading and formatting of graphs, tables, and referencing within the text. The initial mesh of the problem is designed to be as coarse as possible to demonstrate the robustness of Algorithm 4, and show that that the initial element distribution, shown in Fig. 6, is arbitrary when solving fracture problems. Fig. 6 also shows the boundary conditions, the top boundary has a non-zero displacement applied to it whereas the bottom is always fixed. The initial mesh for all problems is constructed from six elements with $p_K = 3 \ \forall K$.

Fig. 7 summarises the global results from the Mode I crack investigation, starting with the overall load–displacement response for the five analyses in Fig. 7(a) which agree well with the benchmark set by Miehe et al. [41], which all show very similar behaviour (the inset figure provides more detail on the peak load–displacement response). The Dirichlet boundary conditions on the top and the bottom of the plate are applied to match the boundary conditions from Miehe et al. [41] so that a validation of the method can be performed. This creates corner singularities in the domain which the adaptive method is able to capture, see the top and bottom corners, on the right, in Fig. 7(d). This is necessary since the damage experienced at the corners will change the load–displacement

Table 1
Mode I crack: simulation identifiers and corresponding parameters.

Simulation	l	h_{min}	TOL_ϕ	TOL_u	Rel. Comp. time	NDOF
A	0.025	0.5l	3.0×10^{-3}	0.05	1	65,775
B	0.025	0.5l	3.0×10^{-3}	inf	0.98	57,387
C	0.025	0.5l	5.0×10^{-3}	inf	0.78	52,329
D	0.025	1.0l	3.0×10^{-3}	inf	0.23	29,925
E	0.025	1.5l	3.0×10^{-3}	inf	0.12	15,696

Fig. 6. Mode I crack: initial mesh with the initial crack edge shown in red. (For interpretation of the references to colour in this figure legend, the reader is referred to the web version of this article.)

response. Applying a roller boundary condition to the top of the domain would remove the corner singularities on the top face, however the singularities at the bottom corners would still exist and influence the result. See Williams [64] for a discussion on singularities at corners at the interface between a homogeneous Neumann and homogeneous Dirichlet boundary condition.

Fig. 7(b) shows how the iteration number, and total load, varies with load step. The load step size is indicated by the width of the bars in the bar chart. The graph shows that the step size algorithm from [39] works well, with the decrease in step size coinciding with the instantaneous fracture. As expected the largest number of iterations occurs during fracture and this stage has both has the highest number of refinement loops and highest iterations per attempted load step.

In order to investigate the time associated with performing extra iterations with the adaptive scheme, a comparison is made between the adaptivity algorithm and an algorithm where no adaptivity is present. The non-adaptive analysis uses the final mesh of the adaptive scheme using Simulation A parameters, where the fixed mesh is shown in Fig. 7(d). The fixed mesh was 6.8 times faster than the adaptive scheme, with 1560 and 12,272 iterations, respectively. Nevertheless, on average each iteration is computationally cheaper for the adaptive scheme. This is also a very severe comparison for the hp-adaptive scheme as in reality such a heavily optimised mesh would not be assumed for a fixed mesh analysis. For this problem with same length scale typical degree of freedom numbers are $\approx 25e3 - 150e3$ DOF [39]. To a perform a less harsh comparison, a mesh with uniform element size and polynomial is considered for a timing test. It has $p_K = 3 \; \forall K \in \mathcal{T}$ and is the result of 6 uniform h-refinements of the mesh in Fig. 6 so the shortest element side lengths are ≈ 0.0156 m, corresponding to $h_{min} = 0.5l$. The uniform mesh
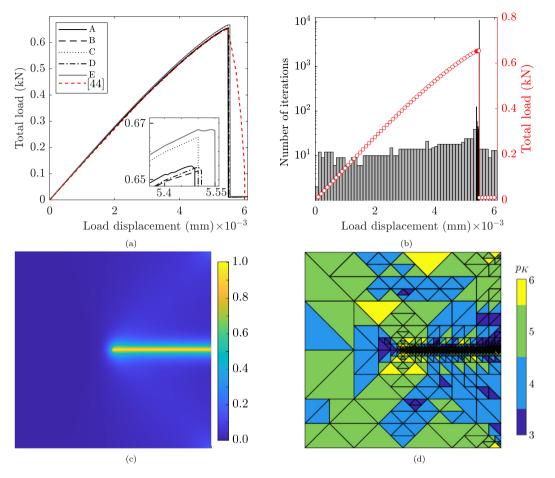
Fig. 7. Mode I crack: (a) load vs. displacement response for all simulations and for Simulation A: (b) the number of BFGS iterations with displacement, (c) final phase field distribution and (d) final mesh.

simulation only required 858 iterations but took 10 times longer than Simulation A, demonstrating the increased speed from an *hp*-adaptivity method when the crack path is unknown.[3]

The final investigation for this problem is how the parameters from Table 1 affect the phase field distribution, shown in Fig. 8. The first observation is that when $h_{min} = 0.5l$, for Simulations A-C, the phase field crack is well formed, with the decrease in error tolerance only causing more refinement away for the crack. The second observation is that even when $h_{min} = 1.5l$ for Simulation E, the phase field is relatively well formed and demonstrates the effect that the higher polynomial is having compared to the polynomial orders typically used in the literature. It is also clear from Fig. 7(a) that the variation in the parameters has little impact on the global force–displacement response. It clearly shows results that would be unobtainable with the same mesh size and elements for $p_K = 1$, moreover it presents a question beyond the scope of this paper; what is the maximum size with arbitrary polynomial order that can achieve an accurate solution of the phase field?

The final mesh, see Fig. 7(d), has small and high polynomial order elements along the crack path and high order elements away from the crack in smooth regions of the solution, such as along the top edge of the domain. These corner singularities have tensile strain components creating values of ≈ 0.2 in the phase field, which smoothly vary away from the corner. This smooth and non-zero region of the phase field solution have sufficiently high errors to require *p*-refinement. Additionally, despite the apparent smoothness, the intermediate solutions, where the global error was deemed too large, can have a very poor phase-field distribution. This could cause *h*- and/or *p*-adaptivity in

---

[3] All timing was performed on a single core of a Intel Xeon Gold 6230 CPU @2.10 GHz with 384 Gb RAM.
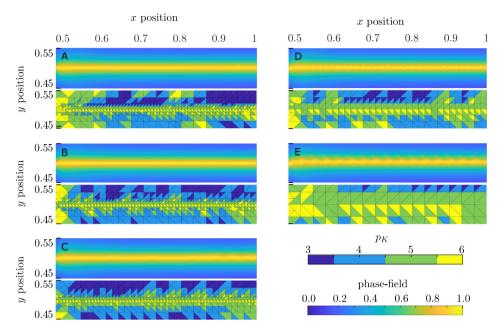
Fig. 8. Mode I crack: expanded view of phase field distribution and final mesh for Simulations A-E.

areas where not entirely necessary. In these cases it is likely that if a derefinement scheme was used these elements would derefine. However, it is not trivial to apply p-derefinement to problems where there are data that need to be preserved, i.e., the history field. When derefining an element, it is desired that the Gauss quadrature is also reduced, however this will prevent the history field distribution from being conserved. It is currently unclear what projection should be used to minimise the loss in history field information. Furthermore, if the Gauss quadrature is maintained such that a low order element has higher than necessary quadrature there is uncertainty in the effect on the runtime. If the runtime has a high dependence on the Gauss quadrature, there may be no advantage to derefine, especially since a higher order element would decrease the global error.

Non-symmetric adaptivity is also observed for this symmetric problem despite having an initially symmetric mesh. This is particularly noticeable on the left hand side of the domain, Fig. 7(d), where an element has $p = 4$ and its symmetric counterpart has $p = 5$. The reason for this difference is that although the initial element topology in the mesh is symmetric, see Fig. 6, the Gauss integration is not. This, in particular, affects the calculation, influence and storage of the history field. Since high order triangular elements are used, a convenient integration scheme is the non-optimal Gauss quadrature presented by Solin [55]. This involves prescribing a square element with the desired Gauss quadrature order, and then mapping this quadrature to the triangular element by moving one corner of the square to its neighbour. The mapping results in Gauss points being clustered towards one corner of the triangle, this therefore leads to a global nonsymmetric Gauss point distribution. Despite this non-symmetry in the numerical integration, the proposed method is able to correctly capture a symmetric crack propagation path due to the hp adaptive scheme.

The cross section of the crack profile described by the phase field is shown in Fig. 9 for simulation parameters from Table 1. The 1D solution on an infinite plate is also included. Around the crack centre all numerical results agree well with the 1D crack solutions, and since the numerical solutions are not on an infinite plate, the further from the crack centre, at $y = 0.5$ m, the further the crack profiles diverge. Generally for all meshes the profile is smooth and any jumps in the DG solution are negligible. Even for simulation E where the minimum element size is limited to 1.5, a good result for the phase-field profile is achieved. Only a slight discrepancy from the other numerical results exists between $y \in [0.5, 0.515]$ m. This demonstrates the capability of high order elements to achieve accurate solutions of the crack profile, reducing the necessity for small elements along the crack edges and tip to achieve an accurate solution.
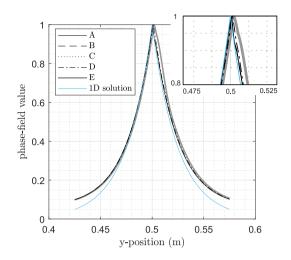
Fig. 9. Mode I crack: The cross section of the phase-field description of the crack at $x = \pi/4$ for the 1D solution for an infinite plate as a reference.

Table 2
Shear crack: simulation identifiers and corresponding parameters.

Simulation	l	h_{min}	TOL_ϕ	TOL_u	Rel. Comp. time	NDOF
A	0.025	0.5l	3.0×10^{-3}	0.05	1	139,845
B	0.025	0.5l	3.0×10^{-3}	inf	0.86	135,381
C	0.025	0.5l	5.0×10^{-3}	inf	0.59	123,348
D	0.025	1.0l	3.0×10^{-3}	inf	0.24	67,626
E	0.025	1.5l	3.0×10^{-3}	inf	0.08	36,969

7.3. Problem 3, shear crack

The shear crack problem is more complex than the uniaxial mode I tensile crack problem as it contains both instantaneous and gradual crack propagation. This generally makes the problem more expensive to solve since in the gradual stage there are more load steps over which small phase field developments occur. Furthermore since the rate of crack propagation is gradual, the rate can have a range of values and is therefore more sensitive to changes in the surrounding mesh. In the instantaneous stage the crack either undergoes significant or zero propagation. The same initial mesh and geometry as used in the previous problem, and shown in Fig. 6, was used for the analyses in this section. For this problem the top boundary condition is set to displace in x only such that $\boldsymbol{g}_D^u = [u_x \ \ 0]$ on $y = 1$ and $\boldsymbol{g}_D^u = [0 \ \ 0]$ on $y = 0$.

Similarly to problem 2, the mode I edge crack, a range of minimum element sizes and error estimate tolerances were considered, as given in Table 2, with the results of the global load versus displacement response shown in Fig. 10(a). The first observation is despite the range of h_{min} values, all of the results are in good agreement. Even for the case where $h_{min} = 1.5l$, Simulation E, all the main features follow approximately the results of Simulation A. These were: At $u \approx 0.01$ mm there is a small instantaneous fracture, producing (i) of Fig. 10(b), followed by a gradual propagation to $u \approx 0.017$ mm, similar to (ii) of Fig. 10(b), concluding with a large drop in the total load when the fracture reaches the bottom boundary, see Fig. 11(a). Additionally, comparison of the phase field distribution of the crack paths between Simulations A and E, shown in Fig. 11(a), demonstrate that the phase field distribution and crack path are in close agreement with Simulation A, albeit less well defined, when considering that the mesh is significantly more coarse, see Fig. 11(b). Similarly to problem 2, the shear crack demonstrates the potential of using coarse meshes in h but with moderate refinement in p.

The variations in the load–displacement responses of the simulations are more easily observed when considering the gradual crack propagation component shown in Fig. 12(a), where the differences in Simulation A and E are more noticeable. However, Simulations A-D are very similar, with the largest outliers being C and D, which are
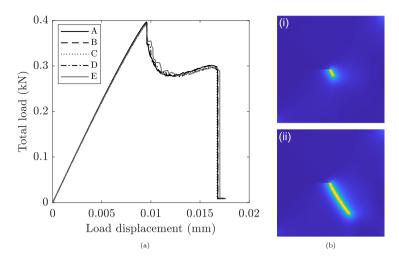
Fig. 10. Shear crack: (a) load versus displacement for all simulations and the phase field development shown in (b).
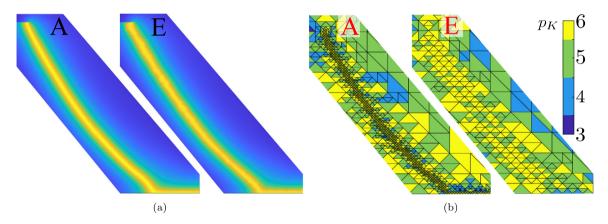

Fig. 11. Shear crack: (a) local phase field distributions for Simulations A and E, and (b) corresponding local mesh.

the simulations with the largest η_ϕ and h_{min}. The difference in response between Simulations A and B is small, indicating that the elasticity error estimate is not necessary here to obtain an accurate response beyond the initial mesh adaptivity required to capture the stress concentration caused by the mesh discontinuity. Overall, despite the range of parameters chosen, all of the simulations provide globally similar force–displacement responses and crack paths, suggesting that reasonable results can be obtained with loose tolerance parameter values.

The variations in the number of iterations and total load, with displacement, are shown in Fig. 12(b) for Simulation A. The overall trend in the iterations is similar to other approaches that use quasi-Newton methods [39,43], with low numbers of iterations per load step during no propagation, $\approx 10 - 30$, higher numbers of iterations for the gradual crack propagation, $\approx 50 - 400$, with the peaks in the number of iterations (≈ 2000) at each instantaneous crack propagation.

A comparison in simulation time was made between Simulation A when using the adaptive method and using a fixed mesh. The fixed mesh is shown in Fig. 13(b) which is the final mesh generated by the adaptive method for Simulation A. In contrast to the problem 2, the adaptive method for the shear crack was 1.15 times faster despite having more iterations than the fixed mesh. The total number of iterations for the adaptive method was 16,073, compared to 8194 for the fixed mesh. Although the number of iterations for the fixed mesh is only half that of the adaptive mesh, the adaptive mesh has far fewer DOF early on in the simulation compared to the latter stages, hence the fixed mesh is solving the problem with far more DOF but with only half as many iterations. It is worth highlighting again that the comparison of an adaptive algorithm with a highly optimised fixed mesh is an extremely
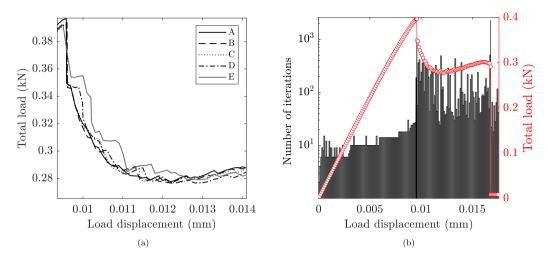
(a)   (b)

Fig. 12. Shear crack: (a) is an expanded view of the total load with displacement curves for all simulations with the corresponding number of iterations for simulation A shown in (b).
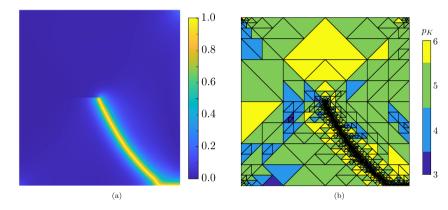

(a)   (b)

Fig. 13. Shear crack: (a) phase field distribution and (b) final refinement mesh.

onerous test on the method developed in this paper as in reality any fixed mesh-based simulation would be far less optimised as the solution path is unknown at the start of the analysis.

The last observation from this section is linked to the final phase field solution and corresponding mesh for Simulation A, shown in Figs. 13(a) and 13(b), respectively. Overall the phase field distribution is nicely formed with the crack also propagating along the bottom boundary. Even though the adaptivity is not driven by phase field values, the *h*-adaptivity is particularly localised to the crack path, varying between 2 or 4 elements wide, noting that the 2 elements width of the smallest length is the highest mesh localisation that is permitted. Away from the phase field crack the solution is smoother and so mostly *p*-refinement was satisfactory to support the elasticity and phase field solutions at the crack. Refinement in the smoother regions away from the crack is necessary so that the total field is represented to a sufficient accuracy to ensure that crack initiation and interaction with the problem boundary is accurate (for example the refinement seen at the corners of the domain not intersected by the crack path).

7.4. Problem 4, two-crack problem

The final problem presented in this paper considers two cracks that are symmetric in their propagation and interaction with each other, where their total propagation is instantaneous. This numerical test is designed push the limits of the algorithm, and set a benchmark in terms of adaptive capability. The geometry, initial mesh, and

Table 3
Two crack: simulation identifiers and corresponding parameters,.

Simulation	l mm	h_{min}	TOL_ϕ	TOL_u	Rel. Comp. time	NDOF	Crack length ratio
A	0.0075	0.5l	0.01	0.05	1.00	181 617	0.99
B	0.0075	0.5l	0.01	inf	1.47	138 027	5.31
C	0.0075	1.0l	0.01	0.05	0.74	123 720	1.01
D	0.0075	1.5l	0.01	0.05	0.45	92 148	1.06
E	0.0075	0.5l	0, $\phi^* = 0.6$	inf	1.39	48 774	36.1
F	0.0075	0.5l	0, $\phi^* = 0.2$	inf	5.7	228 954	52.6

boundary conditions are presented in Fig. 14(a). The mesh is deliberately non symmetric to demonstrate the resultant crack paths are symmetric not because of mesh symmetry, but rather the capability of the proposed error estimator controlled adaptive propagation algorithm.

The problem is difficult to solve because all the crack propagation, and corresponding crack interaction, occurs in a single load step and if the accuracy of the numerical solution is inadequate the final solution will be non-symmetric. With an inadequate adaptive scheme two positive feedback loops will occur:

(i) the mesh-adaptivity could be weighted more towards one crack, increasing the refinement about one crack which then leads to further propagation and refinement for this crack; and

(ii) it is generally observed that in a phase field solution, a crack will propagate down a fine mesh over a coarse mesh, if the adaptivity is poor this will lead to incorrect positioning of the crack path. A poor adaptive algorithm will struggle to recognise that the path is incorrect and the crack propagation will continue in an inappropriate direction.

These problems are compounded by two interacting cracks, where the mesh refinement will directly affect how the cracks will interact, propagate and subsequently how the mesh will be further refined. For this problem the phase field length l was reduced to 0.0075 mm and the minimum step size was set to 1×10^{-4} mm, a series of simulations were run with a range of minimum element sizes and error estimate values, see Table 3. Additionally a comparison of the phase-field results generated by the error estimate driven adaptivity is compared to a result generated by an error indicator driven scheme [65], where the phase-field value is used to drive the adaptivity. This is marked as Simulation E and F in Table 3. In terms of the hp-adaptive algorithm this requires a small change to the definition of the phase field error estimator. For the element K the error $\eta^2_{K,\phi}$ is now a binary value, if K contains at one of its Gauss points $\phi \geq \phi^*$ then $\eta^2_{K,\phi} = 1$. The global error estimator tolerance for the phase field is set to 0, and two phase field threshold values are considered, $\phi^* = 0.6$ (Simulation E) or $\phi^* = 0.2$ (Simulation F). If the phase field in any element contains a value greater than ϕ^* it is h- or p-refined, determined with the smoothness criteria. If no elements in the mesh can be refined further, the load step is considered a success if no element refinements are called.

The results for the total load with displacement are provided in Fig. 14(b). Of these results, Simulations A, C and D created almost symmetric crack propagation, simulation B failed to do this creating non-symmetric cracks of different length, as shown by the crack length ratio in Table 3. Based on the parameters in Table 3, in order to obtain a physically reasonable crack propagation path low values for both η_ϕ and η_u are required. For this problem if η_u is not present the simulation fails. For example, Simulation A creates symmetrically propagating cracks whereas Simulation B does not, where the only difference is that Simulation B does not include elasticity solution error driven mesh refinement. As discussed previously, how well the interaction between the cracks is modelled will affect the final solution, with the interaction influenced by both the accuracy of the phase field and the stress field. To explain this point, the final crack path for Simulation B is provided in Fig. 15. For this two crack problem, the interaction between the cracks and the subsequent propagation is determined by the physical solution more than the previous examples. By not enforcing sufficient accuracy in the displacement solution, the interaction of the stress field between the cracks is insufficient. The remaining simulations are all relatively similar, however the larger the minimum element size and phase field error estimate values, the more nonsymmetric the results become. The ratio between the crack lengths is computed using the integral provided by [41] and provided in Table 3, with Fig. 15 showing how Simulation A is slightly more symmetric than Simulations C and D.
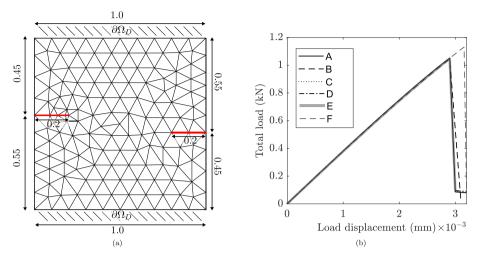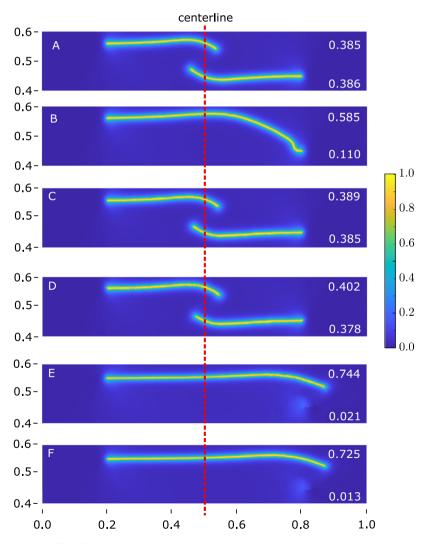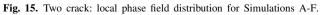
Fig. 14. Two crack: (a) initial mesh and (b) force versus displacement for all simulations.

Fig. 15. Two crack: local phase field distribution for Simulations A-F.
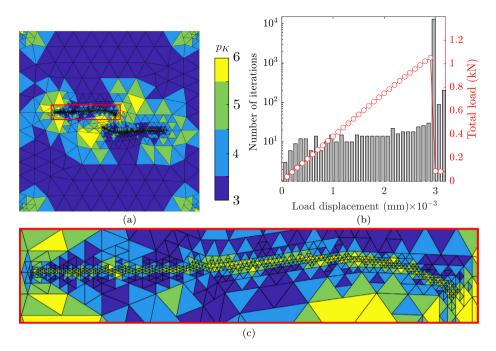
Fig. 16. Two crack, Simulation A: (a) final mesh, (b) number of BFGS iterations and load–displacement response and (c) expanded view of the mesh distribution of the region highlighted by the red box in (a). (For interpretation of the references to colour in this figure legend, the reader is referred to the web version of this article.)

The final mesh for Simulation A is shown in Fig. 16(a), with an expanded view of the mesh around the crack tip, the region marked by the red box in Fig. 16(a), shown in Fig. 16(c). Similar to the single crack problems there is some refinement away from the cracks, in addition there is also more refinement between the cracks compared to other similar regions away from the crack, particularly near the current crack tip positions, indicating that there has been some refinement associated with the interaction between the cracks. Additionally, the expanded view of the crack path shows that the refinement has been localised to the crack path, limited to 2 or 4 elements in width, highlighting that a nearly completely symmetric result has been obtained efficiently with respect to computational effort.

In comparison to Simulations A, C and D, Simulations E and F do not achieve a symmetric crack propagation profile. When the error indicator is based on the values of the phase-field, the refinement is focused on the left hand crack. This is prompted by the initial mesh about the left crack being more refined which then leads to more crack propagation and subsequently further refinement. The simulation highlights that the proposed error estimator has the capability to identify where there should be propagating cracks, since it is able to identify both cracks with a nonsymmetric initial coarse mesh. In addition, particularly for competing and highly interacting cracks, the results show that an error estimator is needed for both the linear elastic field and the phase field. Otherwise symmetric propagation is not achieved. It is remarked that if both cracks had sufficiently small elements about each of the crack tips, then it is more likely that the refinement based indicator for Simulations E and F would be more successful, however this requires some *a priori* knowledge of the solution which is not needed when using the error estimators.

Finally, Fig. 16(b) shows a similar pattern for the number of iterations compared to the mode I crack in Section 7.2. Only when the cracks propagate instantaneously is a high number of iterations observed. Despite the more complex nature of the problem and the smaller l compared to the mode I crack, it is noted that a similar number of iterations, at $\approx 10^4$, occur for the double and mode I tensile crack simulations.

8. Conclusion

Numerous papers have been published that demonstrate the capacity of the phase field approach to model complex fracture propagation in a variety of materials under diverse physical conditions. However, most existing phase field

methods rely on fixed background meshes based on the user's judgement of where they expect fractures to propagate, or a universally fine mesh, both adopting a maximum element size of half of the phase field length parameter, l, in the fracture zones. To resolve this requirement for *a priori* knowledge, both h and hp-adaptive methods have been presented in the literature for phase-field fracture [22,54] with the most popular method to determine where to refine driven by error indicators, based on phase-field values. This paper has presented for the first time a robust residual based *a posteriori hp*-error estimator for the phase field problem, bounding from above and below the error in the energy norm. It is hp since it can be applied to meshes with a range of polynomial orders and robust as it bounds the true error from above and below up to some arbitrary constants. The results for a phase field problem with a known solution show that the efficiency index of the error estimator is about 10. It has the key benefit that no additional numerical solutions are required to determine the error. The advantage of an error estimator is that it will detect regions for refinement where there are low values in the phase-field, this is particularly important for crack initiation and was shown here through the consideration of initial very course meshes. There are methods that do consider residual *a posteriori* error estimators for the phase field [32], however these are limited to h-only. This paper has demonstrated that high order elements around the crack reduce the need for small elements. Good solutions are achieved with side lengths of approximately $1.5l$ and high polynomial orders, up to $p_K = 6$, significantly reducing the computational time and NDOF required.

The error estimator was then coupled with an established elasticity error estimator and an unconstrained optimisation numerical solver to provide an error driven hp-adaptive modelling framework. The numerical examples have shown that it is essential that errors are estimated for both physical equations if robust, initial mesh independent, phase field fracture patterns and realistic global force–displacement responses are to be predicted. In particular it was demonstrated, with the two-crack problem, that when the crack propagation is highly coupled between cracks, it is essential that both error estimators are considered to achieve an accurate solution, otherwise a nonsymmetric crack propagation occurs. Taking advantage of moderate p (up to order 6), as well as h, adaptivity allows element sizes in the vicinity of phase field fractures to be of the order of l whilst obtaining accurate results. The only other approach offering comparable element sizes in this region relies on enrichment [66]. Overall, the method proposed in this paper allows the adoption of arbitrary initial meshes whilst being confident that the final solution will be accurate and independent of the user's knowledge of the expected fracture pattern.

Declaration of competing interest

The authors declare that they have no known competing financial interests or personal relationships that could have appeared to influence the work reported in this paper.

Data availability

All figure data is available at http://dx.doi.org/10.15128/r2pz50gw14x

Acknowledgements

References

[1] Gilles A. Francfort, Jean-Jacques Marigo, Revisiting brittle fracture as an energy minimization problem, J. Mech. Phys. Solids 46 (8) (1998) 1319–1342.

[2] Blaise Bourdin, Gilles A. Francfort, Jean-Jacques Marigo, Numerical experiments in revisited brittle fracture, J. Mech. Phys. Solids 48 (4) (2000) 797–826.

[3] Christian Miehe, Fabian Welschinger, Martina Hofacker, Thermodynamically consistent phase-field models of fracture: Variational principles and multi-field FE implementations, Internat. J. Numer. Methods Engrg. 83 (10) (2010) 1273–1311.

[4] Adriana Paluszny, Robert W. Zimmerman, Numerical simulation of multiple 3D fracture propagation using arbitrary meshes, Comput. Methods Appl. Mech. Engrg. 200 (9–12) (2011) 953–966.

[5] Christian Miehe, Ercan Gürses, A robust algorithm for configurational-force-driven brittle crack propagation with r-adaptive mesh alignment, Internat. J. Numer. Methods Engrg. 72 (2) (2007) 127–155.

[6] Michael J Borden, Clemens V Verhoosel, Michael A Scott, Thomas JR Hughes, Chad M Landis, A phase-field description of dynamic brittle fracture, Comput. Methods Appl. Mech. Engrg. 217 (2012) 77–95.

[7] Robert E. Bird, A hp-adaptive discontinuous Galerkin finite element method for accurate configurational force brittle crack propagation (Ph.D. thesis), Durham University, 2020.

[8] Xiangming Sun, Ravindra Duddu, Hirshikesh Hirshikesh, A poro-damage phase field model for hydrofracturing of glacier crevasses, Extreme Mech. Lett. 45 (2021) 101277.

[9] Theo Clayton, Ravindra Duddu, Martin Siegert, Emilio Martí nez Pañeda, A stress-based poro-damage phase field model for hydrofracturing of creeping glaciers and ice shelves, Eng. Fract. Mech. 272 (2022) 108693.

[10] P. Areias, T. Rabczuk, M.A. Msekh, Phase-field analysis of finite-strain plates and shells including element subdivision, Comput. Methods Appl. Mech. Engrg. 312 (2016) 322–350.

[11] Alba Muixí, Antonio Rodríguez-Ferran, Sonia Fernández-Méndez, A hybridizable discontinuous Galerkin phase-field model for brittle fracture with adaptive refinement, Internat. J. Numer. Methods Engrg. 121 (6) (2020) 1147–1169.

[12] Hojjat Badnava, Mohammed A. Msekh, Elahe Etemadi, Timon Rabczuk, An h-adaptive thermo-mechanical phase field model for fracture, Finite Elem. Anal. Des. 138 (2018) 31–47.

[13] Abhinav Gupta, U. Meenu Krishnan, Rajib Chowdhury, Anupam Chakrabarti, An auto-adaptive sub-stepping algorithm for phase-field modeling of brittle fracture, Theor. Appl. Fract. Mech. 108 (2020) 102622.

[14] Davide Proserpio, Marreddy Ambati, Laura De Lorenzis, Josef Kiendl, A framework for efficient isogeometric computations of phase-field brittle fracture in multipatch shell structures, Comput. Methods Appl. Mech. Engrg. 372 (2020) 113363.

[15] Nima Noii, Fadi Aldakheel, Thomas Wick, Peter Wriggers, An adaptive global–local approach for phase-field modeling of anisotropic brittle fracture, Comput. Methods Appl. Mech. Engrg. 361 (2020) 112744.

[16] Davide Proserpio, Marreddy Ambati, Laura De Lorenzis, Josef Kiendl, A framework for efficient isogeometric computations of phase-field brittle fracture in multipatch shell structures, Comput. Methods Appl. Mech. Engrg. 372 (2020) 113363.

[17] Timo Heister, Mary F. Wheeler, Thomas Wick, A primal-dual active set method and predictor-corrector mesh adaptivity for computing fracture propagation using a phase-field approach, Comput. Methods Appl. Mech. Engrg. 290 (2015) 466–495.

[18] Nima Noii, Thomas Wick, A phase-field description for pressurized and non-isothermal propagating fractures, Comput. Methods Appl. Mech. Engrg. 351 (2019) 860–890.

[19] Markus Klinsmann, Daniele Rosato, Marc Kamlah, Robert M McMeeking, An assessment of the phase field formulation for crack growth, Comput. Methods Appl. Mech. Engrg. 294 (2015) 313–330.

[20] Abhinav Gupta, U. Meenu Krishnan, Tushar Kanti Mandal, Rajib Chowdhury, Vinh Phu Nguyen, An adaptive mesh refinement algorithm for phase-field fracture models: Application to brittle, cohesive, and dynamic fracture, Comput. Methods Appl. Mech. Engrg. (ISSN: 0045-7825) 399 (2022) 115347.

[21] U. Meenu Krishnan, Abhinav Gupta, Rajib Chowdhury, Adaptive phase-field modeling of brittle fracture using a robust combination of error-estimator and markers, Eng. Fract. Mech. 274 (2022) 108758.

[22] H. Hirshikesh, A.L.N. Pramod, Haim Waisman, S. Natarajan, Adaptive phase field method using novel physics based refinement criteria, Comput. Methods Appl. Mech. Engrg. 383 (2021) 113874.

[23] Alba Muixí, Onofre Marco, Antonio Rodríguez-Ferran, Sonia Fernández-Méndez, A combined XFEM phase-field computational model for crack growth without remeshing, Comput. Mech. 67 (2021) 231–249.

[24] Yi Jin, OA González-Estrada, O Pierard, SPA3627181 Bordas, Error-controlled adaptive extended finite element method for 3D linear elastic crack propagation, Comput. Methods Appl. Mech. Engrg. 318 (2017) 319–348.

[25] Xiaobing Feng, Hai-jun Wu, A posteriori error estimates and an adaptive finite element method for the allen–cahn equation and the mean curvature flow, J. Sci. Comput. 24 (2005) 121–146.

[26] Chintan Jansari, K Kannan, RK Annabattula, S Natarajan, et al., Adaptive phase field method for quasi-static brittle fracture using a recovery based error indicator and quadtree decomposition, Eng. Fract. Mech. 220 (2019) 106599.

[27] Emilio Martínez-Pañeda, Sundararajan Natarajan, et al., Adaptive phase field modelling of crack propagation in orthotropic functionally graded materials, Def. Technol. 17 (1) (2021) 185–195.

[28] Somdatta Goswami, Cosmin Anitescu, Timon Rabczuk, Adaptive phase field analysis with dual hierarchical meshes for brittle fracture, Eng. Fract. Mech. 218 (2019) 106608.

[29] Olgierd C. Zienkiewicz, Jian Z. Zhu, A simple error estimator and adaptive procedure for practical engineerng analysis, Internat. J. Numer. Methods Engrg. 24 (2) (1987) 337–357.

[30] Thomas Wick, Goal functional evaluations for phase-field fracture using PU-based DWR mesh adaptivity, Comput. Mech. 57 (6) (2016) 1017–1035.

[31] Rolf Mahnken, Goal-oriented adaptive refinement for phase field modeling with finite elements, Internat. J. Numer. Methods Engrg. 94 (4) (2013) 418–440.

[32] Katrin Mang, Mirjam Walloth, Thomas Wick, Winnifried Wollner, Mesh adaptivity for quasi-static phase-field fractures based on a residual-type a posteriori error estimator, GAMM-Mitt. 43 (1) (2020) e202000003.

[33] Siobhan Burke, Christoph Ortner, Endre Süli, An adaptive finite element approximation of a variational model of brittle fracture, SIAM J. Numer. Anal. 48 (3) (2010) 980–1012.

[34] Siobhan Burke, Christoph Ortner, Endre Sueli, An adaptive finite element approximation of a generalized Ambrosio–Tortorelli functional, Math. Models Methods Appl. Sci. 23 (09) (2013) 1663–1697.

[35] Stefano Micheletti, Simona Perotto, Marianna Signorini, Anisotropic mesh adaptation for the generalized ambrosio–tortorelli functional with application to brittle fracture, Comput. Math. Appl. 75 (6) (2018) 2134–2152, 2nd Annual Meeting of SIAM Central States Section, September 30-October 2, 2016.

[36] Robert E. Bird, William M. Coombs, Stefano Giani, A posteriori discontinuous Galerkin error estimator for linear elasticity, Appl. Math. Comput. 344–345 (2019) 78–96.

[37] Leszek F. Demkowicz, Jay Gopalakrishnan, An overview of the discontinuous Petrov Galerkin method, in: Recent Developments in Discontinuous Galerkin Finite Element Methods for Partial Differential Equations: 2012 John H Barrett Memorial Lectures, Springer, 2014, pp. 149–180.

[38] Leszek Demkowicz, Jay Gopalakrishnan, Discontinuous Petrov–Galerkin (DPG) method, ICES Rep. 15 (2015).

[39] Philip K. Kristensen, Emilio Martínez-Pañeda, Phase field fracture modelling using quasi-Newton methods and a new adaptive step scheme, Theor. Appl. Fract. Mech. 107 (2020) 102446.

[40] Tymofiy Gerasimov, Laura De Lorenzis, A line search assisted monolithic approach for phase-field computing of brittle fracture, Comput. Methods Appl. Mech. Engrg. 312 (2016) 276–303.

[41] Christian Miehe, Martina Hofacker, Fabian Welschinger, A phase field model for rate-independent crack propagation: Robust algorithmic implementation based on operator splits, Comput. Methods Appl. Mech. Engrg. 199 (45–48) (2010) 2765–2778.

[42] Patrick Farrell, Corrado Maurini, Linear and nonlinear solvers for variational phase-field models of brittle fracture, Internat. J. Numer. Methods Engrg. 109 (5) (2017) 648–667.

[43] Jian-Ying Wu, Yuli Huang, Vinh Phu Nguyen, On the BFGS monolithic algorithm for the unified phase field damage theory, Comput. Methods Appl. Mech. Engrg. 360 (2020) 112704.

[44] Ritukesh Bharali, Somdatta Goswami, Cosmin Anitescu, Timon Rabczuk, A robust monolithic solver for phase-field fracture integrated with fracture energy based arc-length method and under-relaxation, Comput. Methods Appl. Mech. Engrg. 394 (2022) 114927.

[45] Tushar Kanti Mandal, Abhinav Gupta, Vinh Phu Nguyen, Rajib Chowdhury, Alban de Vaucorbeil, A length scale insensitive phase field model for brittle fracture of hyperelastic solids, Eng. Fract. Mech. 236 (2020) 107196.

[46] Daniel Jodlbauer, Ulrich Langer, Thomas Wick, Matrix-free multigrid solvers for phase-field fracture problems, Comput. Methods Appl. Mech. Engrg. 372 (2020) 113431.

[47] Lampros Svolos, Luc Berger-Vergiat, Haim Waisman, Updating strategy of a domain decomposition preconditioner for parallel solution of dynamic fracture problems, J. Comput. Phys. 422 (2020) 109746.

[48] Vinamra Agrawal, Brandon Runnels, Block structured adaptive mesh refinement and strong form elasticity approach to phase field fracture with applications to delamination, crack branching and crack deflection, Comput. Methods Appl. Mech. Engrg. 385 (2021) 114011.

[49] Ran Ma, WaiChing Sun, FFT-based solver for higher-order and multi-phase-field fracture models applied to strongly anisotropic brittle materials, Comput. Methods Appl. Mech. Engrg. 362 (2020) 112781.

[50] Alba Muixi, Antonio Rodriguez-Ferran, Sonia Fernandez-Mendez, A hybridizable discontinuous Galerkin phase-field model for brittle fracture with adaptive refinement, Internat. J. Numer. Methods Engrg. 121 (6) (2020) 1147–1169.

[51] Prashant Mital, Thomas Wick, Mary F Wheeler, Gergina Pencheva, Discontinuous and enriched Galerkin methods for phase-field fracture propagation in elasticity, in: Numerical Mathematics and Advanced Applications ENUMATH 2015, Springer, 2016, pp. 195–203.

[52] Lampros Svolos, Hashem M. Mourad, Gianmarco Manzini, Krishna Garikipati, A fourth-order phase-field fracture model: Formulation and numerical solution using a continuous/discontinuous Galerkin method, J. Mech. Phys. Solids 165 (2022) 104910.

[53] Sindhu Nagaraja, Mohamed Elhaddad, Marreddy Ambati, Stefan Kollmannsberger, Laura De Lorenzis, Ernst Rank, Phase-field modeling of brittle fracture with multi-level hp-FEM and the finite cell method, Comput. Mech. 63 (6) (2019) 1283–1300.

[54] Lisa Hug, Stefan Kollmannsberger, Zohar Yosibash, Ernst Rank, A 3D benchmark problem for crack propagation in brittle fracture, Comput. Methods Appl. Mech. Engrg. 364 (2020) 112905.

[55] Pavel Solin, Karel Segeth, Ivo Dolezel, Higher-Order Finite Element Methods, CRC Press, 2003.

[56] Davide D'Angella, Stefan Kollmannsberger, Ernst Rank, Alessandro Reali, Multi-level bézier extraction for hierarchical local refinement of isogeometric analysis, Comput. Methods Appl. Mech. Engrg. 328 (2018) 147–174.

[57] Paolo Di Stolfo, Andreas Schröder, Nils Zander, Stefan Kollmannsberger, An easy treatment of hanging nodes in hp-finite elements, Finite Elem. Anal. Des. (ISSN: 0168-874X) 121 (2016) 101–117.

[58] Tino Eibner, Jens Markus Melenk, An adaptive strategy for hp-FEM based on testing for analyticity, Comput. Mech. 39 (5) (2007) 575–595.

[59] Marreddy Ambati, Tymofiy Gerasimov, Laura De Lorenzis, A review on phase-field models of brittle fracture and a new fast hybrid formulation, Comput. Mech. 55 (2) (2015) 383–405.

[60] Serge Prudhomme, Frédéric Pascal, John T. Oden, Albert Romkes, Review of a priori error estimation for discontinuous Galerkin methods. TICAM report 00–27, Tex. Inst. Comput. Appl. Math. (2000).

[61] Jorge Nocedal, Updating quasi-Newton matrices with limited storage, Math. Comp. 35 (151) (1980) 773–782.

[62] John E. Dennis Jr., Robert B. Schnabel, Numerical Methods for Unconstrained Optimization and Nonlinear Equations, SIAM, 1996.

[63] Robert Bird, William M. Coombs, Stefano Giani, Accurate configuration force evaluation via hp-adaptive discontinuous Galerkin finite element analysis, Eng. Fract. Mech. (2019) 106370.

[64] Max L. Williams, Stress singularities resulting from various boundary conditions in angular corners of plates in extension, 1952.

[65] Alba Muixí, Sonia Fernández-Méndez, Antonio Rodríguez-Ferran, Adaptive refinement for phase-field models of brittle fracture based on nitsche's method, Comput. Mech. 66 (1) (2020) 69–85.

[66] Stefan Loehnert, Christian Krüger, Verena Klempt, Lukas Munk, An enriched phase-field method for the efficient simulation of fracture processes, Comput. Mech. (2023).